5-2019

Studies of Molecular Magnetism and Dynamics by Inelastic Neutron Scattering and Nuclear Magnetic Resonance

Zhiming Liu
University of Tennessee, zliu40@vols.utk.edu

Studies of Molecular Magnetism and Dynamics by Inelastic Neutron Scattering and Nuclear Magnetic Resonance

A Thesis Presented for the

Master of Science

Degree

The University of Tennessee, Knoxville

Zhiming Liu

May 2019

Dedication

To my grandmother

who enlightened me

to explore different possibilities of the life.

Acknowledgement

I would like to thank my advisor Dr. Ziling (Ben) Xue who provided me with this precious opportunity for studying here. I thank him for the guidance, support and letting me know how to be a dedicated researcher. I would like to acknowledge Dr. Sheng Dai, Dr. Michael Best and Dr. Konstantinos Vogiatzis for helping me during my time in graduate school. I especially appreciate Dr. Carlos Steren for his time and advice on NMR techniques.

I would like to thank Dr. Luke Daemen, Dr. Yongqiang Cheng and Dr. Andrey Podlesnyak at Oak Ridge National Laboratory, Dr. Wei Zhou at NIST Center for Neutron Research, Dr. Jurek Krzystek at National High Magnetic Field Laboratory, Dr. Joshua Telser at Roosevelt University, and Dr. Haidong Zhou at the University of Tennessee-Knoxville for collaboration, including data collection and analysis. Dr. Xuetai Chen and his research group at Nanjing University are also acknowledged for providing the samples in Chapter 3.

I would like to thank Dr. Shelby Stavretis for sharing her neutron scattering knowledge and data analysis skills with me. I thank Duncan Moseley, Clay Mings, Chelsea Widener, Alex Bone, Brian Kettell, Pagnareach Tin, Evan Lewoczko, Bryan Casale, Jinchao Lou, Xinyi Wang, Kiu Chui, and Hsin-Hui Chang for their help during my time here. I am especially thankful for Peter Pham who provided me with tremendous help to overcome the language barrier.

This journey would not have been possible without the support of my family. To my family, thank you for encouraging me in all of my pursuits and inspiring me to follow my dreams.

Abstract

This thesis is mainly focused on studying molecular magnetism by inelastic neutron scattering (INS) and nuclear magnetic resonance (NMR) spectroscopy. Other techniques such as high-frequency electron paramagnetic resonance (HF-EPR) and DC magnetic susceptibility are also utilized to provide more comprehensive understanding. The sign and magnitude of axial zero-field splitting parameter *D* of Mn(TPP)X (H_2TPP = tetraphenylporphyrin; X = Br and I) have been directly determined by INS and are consistent with the measurement of HF-EPR. Mn(TPP)F is EPR silent in both solid (5-290 K) and frozen solution (10 K in chloroform) state, making it different from its Br and I analogies. Studies of Mn(TPP)F suggest that molecules form a 1-D chain structure in solid-state through F^- bridges, but extended research is needed to support this hypothesis. Ligand effect of a series of pseudo-tetrahedral Co^{II} [positive two cobalt ion] complexes $Co(EPh_3)_2X_2$ [cobalt triphenylphosphine chlorine] (E = P, X = CI, Br, I; E = As, X = I) was studied by variable-temperature and variable-magnetic-field INS. In this pseudo-tetrahedral Co^{II} system, the anisotropy barriers do not change notably when the coordinating halide ligands change from lighter Cl to heaver Br and I. However, a significant increase of the axial anisotropy 2*D* value appears when substituting the phosphine with the arsine ligand. This work demonstrated that INS can provide opportunities to precisely probe the anisotropy barrier when it exceeds the range of HF-EPR. In addition, dynamics of group 10 metal complexes with macrocyclic amine N-heterocyclic carbene (NHC) ligands was studied by NMR.

Table of Contents

List of Tables

List of Figures

List of Complexes

1	$Mn(TPP)Br$	(H_2TPP = tetraphenylporphyrin)
2	$Mn(TPP)I$	
3	$Mn(TPP)F$	
4	$Co(PPh_3)_2Cl_2$	
5	$Co(PPh_3)_2Br_2$	
6	$Co(PPh_3)_2I_2$	
7	$Co(AsPh_3)_2I_2$	
8	$[NiL^1][PF_6]_2$	(Structure of $[H_2L^1]$ is shown in **Figure 4.1**)
9	$[PdL^1][PF_6]_2$	
10	$[PtL^1][PF_6]_2$	
11	$[NiL^2][PF_6]_2$	(Structure of $[H_2L^2]$ is shown in **Figure 4.1**)
12	$[PdL^2][PF_6]_2$	
13	$[PtL^2][PF_6]_2$	
14	$[Pd(L^2)(acac)]$	(acac = acetylacetonate)

1. Introduction

1.1 Molecular magnetism

Magnets have been known for over 2000 years and are still playing an extraordinary role in countless technological applications that pass through daily life. Traditionally, magnets are strongly correlated to metals, intermetallic alloy, and their oxides.[1] Neodymium magnets ($Nd_2Fe_{14}B$), which were discovered in 1980s by Sumitomo Special Metals and General Motors, are one of the strongest and most widely used permanent rare-earth magnets.[2] The flourish of miniaturization technologies requires molecular magnetic materials with sophisticated properties for information storage, molecular sensor, and spintronics devices. Single-molecule magnets (SMMs), a class of superparamagnetic molecules exhibiting magnetic bistability behaviors individually under the critical temperature, have the potential to meet these requirements.[3] Usually an SMM contains one or more transition- or lanthanide-metal ions surrounded by organic ligands. The ligands separate and prevent metals from interacting with each other. No long-range interaction is needed to retain the magnetic properties, making SMMs likely the upper limit of the high-density information storage materials. SMMs have been actively studied over the past two decades by both chemists and physicists. The first SMM reported in early 1990s is a cluster containing 12 Mn ions that exhibits slow relaxation under 4 K.[4-5] About 3 decades later, the blocking temperature of SMMs was reported to be above 77 K for the first time.[6-7] These achievements are a milestone of the SMM field and have opened doors to the future development of practical data storage devices and microprocessors in quantum computers.

1.1.1 Magnetic anisotropy

To make a molecule function as a magnet, a large magnetic anisotropy barrier is needed to prevent the magnetic moment to re-orientate between “up” and “down” after being removed from the magnetic field.[8] The efficiency of molecules to maintain their magnetization is denoted by effective spin-reversal magnetic anisotropy energy barrier (U_{eff}). U_{eff} of the central ion is closely related to the molecule’s individual intrinsic electronic structure (coordination environment) and originates differently for transition and lanthanide metals.

For transition metal-based SMMs, the electronic structure of the central ion is determined by Coulombic interaction, crystal-field (CF) interaction, and spin-orbit coupling (SOC) (**Figure 1.1 (Left)**). The strong interaction between d-orbitals and the ligand field could lead to the quenching of the ground-state orbital angular momentum, which results in the invalidation of the first-order SOC. In this case, the magnetic anisotropy arises from the second-order SOC, which also known as zero-field splitting (ZFS). ZFS is the interaction of energy levels of a metal ion with more than one unpaired electron and quenched orbital motions. Second-order SOC introduces small amount of orbital angular momentum by mixing the ground state with the excited states. Thus, ZFS is sensitive to both electronic spin and the coordination environment.[9] The ZFS interaction Hamiltonian is expressed in **Eq. 1.1.**

$$\widehat{H} = D\left[\hat{S}_z^2 - \frac{S(S+1)}{3}\right] + E(\hat{S}_x^2 - \hat{S}_y^2) \qquad \textbf{(Eq. 1.1)}$$

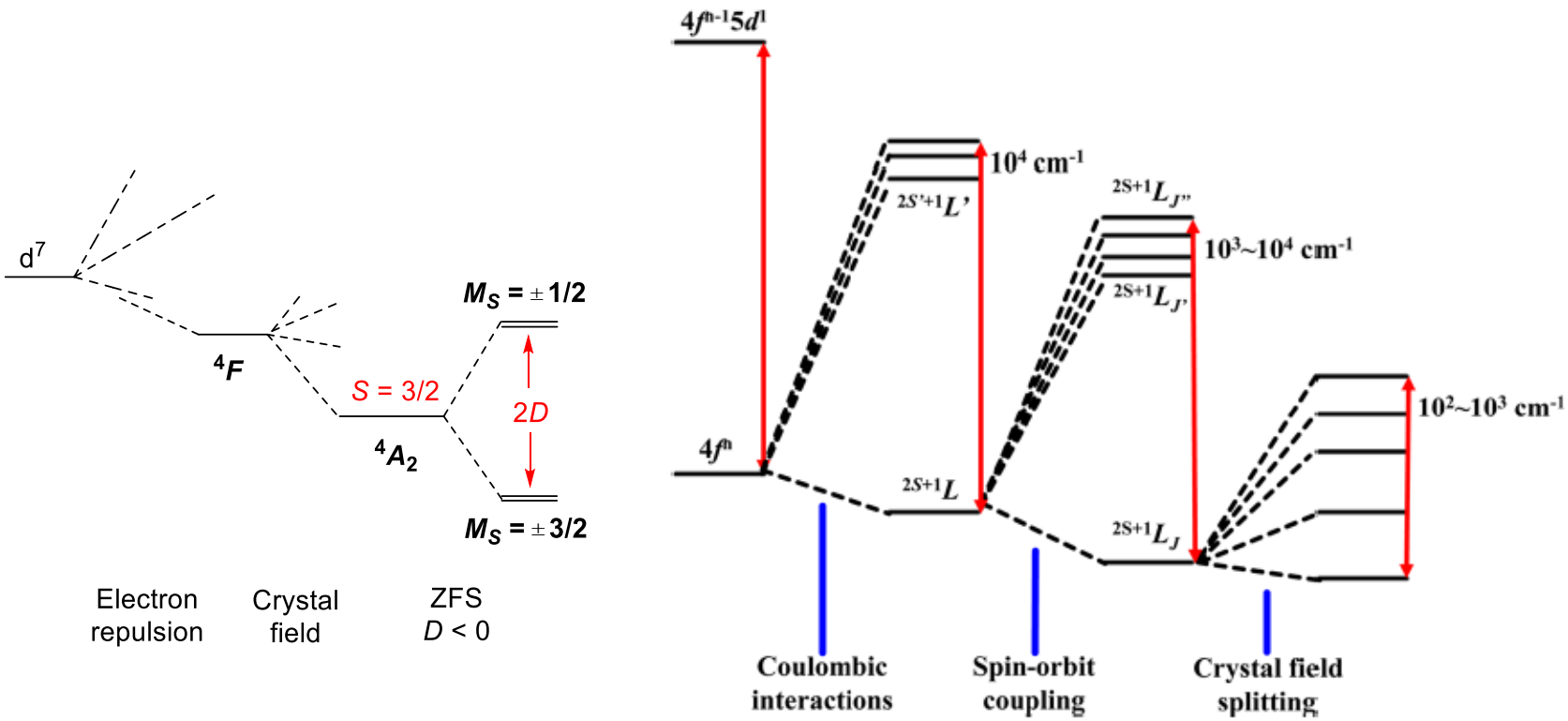

Figure 1.1 Energy splitting schematic diagrams of examples of in high-spin, 4-coordinated, C_{2v}, d^7 transition-metal complexes (Left) and lanthanide (Right) metal-based SMMs.

D and *E* are axial and rhombic zero-field splitting parameters respectively, they describe the extent of ZFS splitting in axial and rhombic directions. $\hat{S}$ is the spin projection in a given direction and *S* is the total spin. The effective energy barrier is denoted as U_{eff}, which is given by:

For integer spin system:

$$U_{eff} = |D| \cdot S^2 \qquad \textbf{(Eq. 1.2a)}$$

For half-integer spin system:

$$U_{eff} = |D| \cdot (S^2 - 1/4) \qquad \textbf{(Eq. 1.2b)}$$

For lanthanide metal-based SMMs, f-orbitals are deeply buried and experience weaker influence from CF. The near degenerate f-orbitals make SOC more important than CF in describing its electronic structure (**Figure 1.1 (Right)**)[10]. As a consequence, the energy levels of lanthanide metal-based SMMs are less sensitive to the environment. The ground state term symbols ($^{2S+1}L_J$) of Ln ions can be determined by Russell-Saunders coupling scheme and Hund's Rule. Take one of the most extensively studied Ln ions Dy(III) as an example, its free ion ground state term $^6H_{15/2}$ has sixteen-fold degenerate M_J states and these M_J states can be affected differently by the symmetry and strength of the CF and eventually split into eight Kramers doublets. In order to obtain a larger U_{eff}, the ground state M_J should be doubly degenerate and have a large energy gap between this ground state and its first excited state.[11] These properties could be achieved through engineering its coordination environment.

1.1.2 Magnetic relaxations

Having a large magnetic anisotropy barrier is critical to SMMs, but relaxation mechanisms could shortcut this barrier and reverse the magnetization even when the thermal energy (K_BT) of the environment is less than the magnetic energy level separation (U). Two factors that are related to the magnetic moment re-orientation are: spin-lattice relaxation and quantum tunneling magnetization (QTM).

Four relaxation processes are described in **Eq. 1.3**. The first three terms are spin-phonon coupling mechanism and the last term is QTM. Spin-phonon coupling is the process where the magnetic ion (spin) interacts with the lattice vibration (phonons) by exchanging energies. As expressed in **Figure 1.2**, these four mechanisms are: (1) Direct relaxation is a single-phonon process that changes M_J from excited to ground states. This mechanism mainly occurs at low temperature. (2) Orbach relaxation is a double-phonon process where the energy difference of two phonons matches the energy gap between M_J states. In contrast to direct relaxation, this process is dominant at higher temperature. (3) Raman relaxation is another double-phonon process which is similar to the Orbach relaxation, but the superposed phonons in the Raman process are at virtual states instead.[11-12] The last term in **Eq. 1.3**. describes QTM. A strong QTM effect can be observed if the rhombic anisotropy of the system is large. The QTM effect between two superposed M_J states greatly weaken the effective anisotropy barrier. Typically, a weak static magnetic field could break the superposition of M_J states and suppress the QTM. However, we do see exceptions where QTM is enhanced by the static magnetic field.[13] Its detailed mechanism is yet to be fully understood. The contributions of these mechanisms are defined from the AC magnetic susceptibility fitting of **Eq. 1.3**.

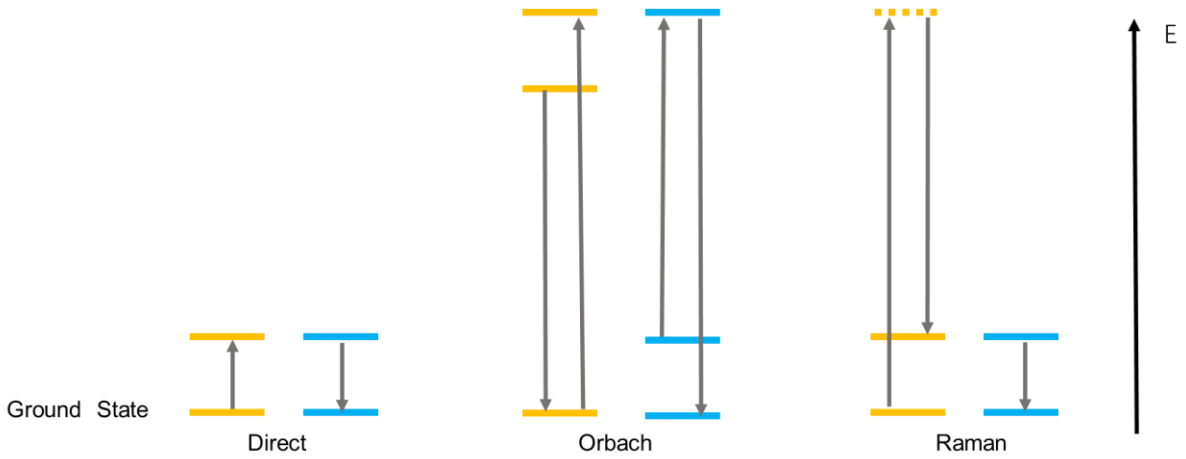

Figure 1.2 Schematic overview of the different relaxation mechanisms. Yellow lines indicate phonon levels, while blue lines indicate $\pm M_J$ ($\pm M_S$) states.

$$\tau^{-1} = AH^{n_1}T + CT^{n_2} + \tau_0^{-1}\exp\left(-\frac{\Delta_{CF}}{k_BT}\right) + \frac{B_1}{(1+B_2H^2)} \qquad \textbf{(Eq. 1.3)}$$

where τ is the relaxation time; *H* is the applied field; Δ_{CF} represents the energy gap between the ground and excited state; A–C and τ_0 are free fit parameters; n_1 and n_2 are values that can be found in the literature.[14]

1.2 Inelastic neutron scattering

As mentioned before, the fitting of AC susceptibility data has been extensively used to determine the effective magnetic anisotropy energy barrier. However, this indirect method could lead to errors in *D* and *E* values due to the presence of multiple fitting parameters. The precise determination of the magnetic energy level separation that exceed the range of HF-EPR is a challenge in SMM research. Inelastic neutron scattering (INS) is one of the few techniques that can measure this separation directly.

1.2.1 Inelastic Neutron Scattering to probe molecular magnetism

Neutrons are neutral particles that carry magnetic moments (spin = 1/2). Typically, when shooting neutron beams through samples, neutrons can be scattered by nuclei of atoms through strong nuclear force interaction. If the sample has unpaired electrons, the magnetic field of unpaired electrons can interact with the magnetic moment of neutrons and lead to magnetic scattering. This process provides an opportunity to measure the transitions between different magnetic levels directly. The kinetic information of incident and scattered neutron is described as initial wave vector $\boldsymbol{k}_i$ and finial wave vector $\boldsymbol{k}_f$. As shown in **Figure 1.3**, in the inelastic scattering process, an incident neutron will change its energy and direction during the interaction with the target. Momentum transfer $\boldsymbol{Q}$ can be calculated by $\boldsymbol{Q} = \boldsymbol{k}_i - \boldsymbol{k}_f$.

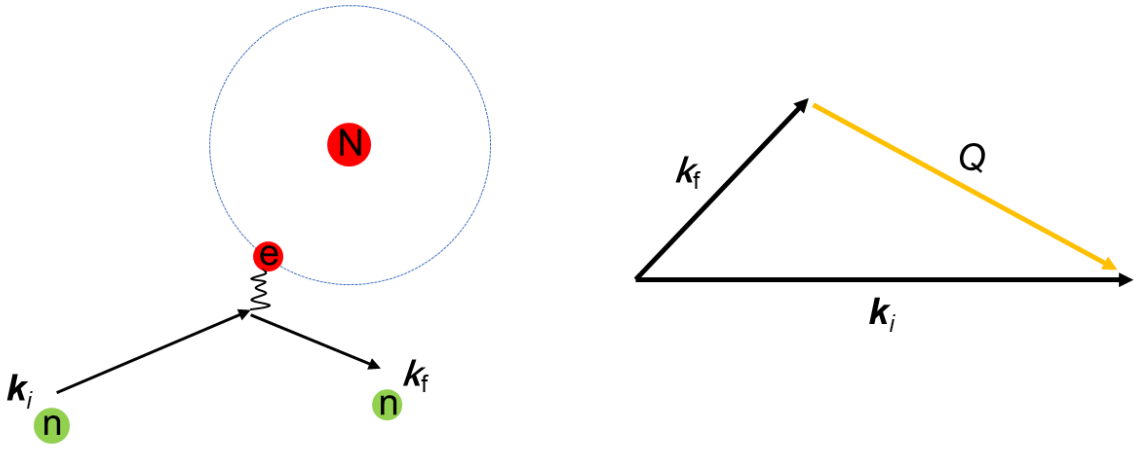

Figure 1.3 Neutron interacts with unpaired electron through magnetic dipole-dipole interaction (Left). Scattering triangle of inelastic neutron scattering (Right).

Based on the magnetic form factor, the intensity of magnetic scattering falls off with the increase of momentum transfer (***Q***) while the intensity of vibrational originated peaks decreases.[15] Therefore, magnetic scattering is typically probed at low ***Q*** and phonons are measured at high ***Q***. However, incoherent scattering from ligand atoms, especially from H atoms, causes strong unconstructed background noises and occasionally overwhelms the magnetic signal. Thus, deuteron is often used to substitute hydrogen in INS samples to improve the single-to-noise ratio. Magnetic signals can also be overwhelmed by phonons when magnetic peaks are in the high energy region where phonon density of states is large. It is difficult to distinguish magnetic versus phonon signals in INS.

There are several methods to reveal magnetic transitions from phonons. Variable-temperature INS and variable-magnetic field INS are two methods that have been applied for this work:

(1) The intensity of magnetic peaks is based on Boltzmann distribution. Thus, the intensity of magnetic peaks should decrease as the temperature increases. The temperature dependence of phonon peaks is removed by Bose-correction (**Eq. 1.4**).

$$f_{corrected}(E) = \frac{1-\exp\left(\frac{-2E}{k_b T}\right)}{1+\exp\left(\frac{-2E}{k_b T}\right)} \times f(E) \quad \textbf{(Eq. 1.4)}$$

where $f_{corrected}(E)$ is the corrected scattering intensity, *E* is the incident neutron energy, k_b is the Boltzmann constant, and $f(E)$ is the original intensity. As a result, phonon intensity should remain the same under different temperatures in the Bose-corrected spectra.

(2) Magnetic energy levels experience Zeeman splitting under the applied magnetic

field. Therefore, peaks of magnetic origin shift to higher energy with increased applied field while peaks of vibrational origin remain in a fixed position.

1.2.2 Spectrometers for neutron scattering

INS can be used for probing a variety of properties of the materials with a wide range of time and length scales. It offers possibilities to reveal unique physical and chemical phenomena. Cold neutron (0–25 meV)[16] inelastic scattering is ideal for studying low-lying energy levels. Compared to optical spectroscopies like IR and Raman, INS does not have symmetry selection rules. All allowed transitions can be revealed by INS. Therefore, it can give a more comprehensive spectroscopic characterization of the sample.[17] Three different spectrometers are used in this work. These spectrometers are recently reviewed.[18]

Disk Chopper Spectrometer (DCS)[19] is a direct geometry TOF chopper spectrometer at the NIST Center for Neutron Research (NCNR), National Institute of Standards and Technology (NIST). As shown in **Figure 1.4 (Top)**, a white neutron beam from the source was filtered by a set of choppers before interacting with the target. The detector bank covers a wide range of angles, which gives rich information of ***Q***. DCS provides a flexible choice of incident energies and resolutions. The wavelength of the incident beam can be tuned from 8 to at least 200 cm^{-1}.[20] The 10-T magnet is the largest among the neutron sources in the U.S. Both variable-temperature and variable-magnetic field INS are feasible with DCS.

Cold Neutron Chopper Spectrometer (CNCS)[21] is a high-resolution, direct

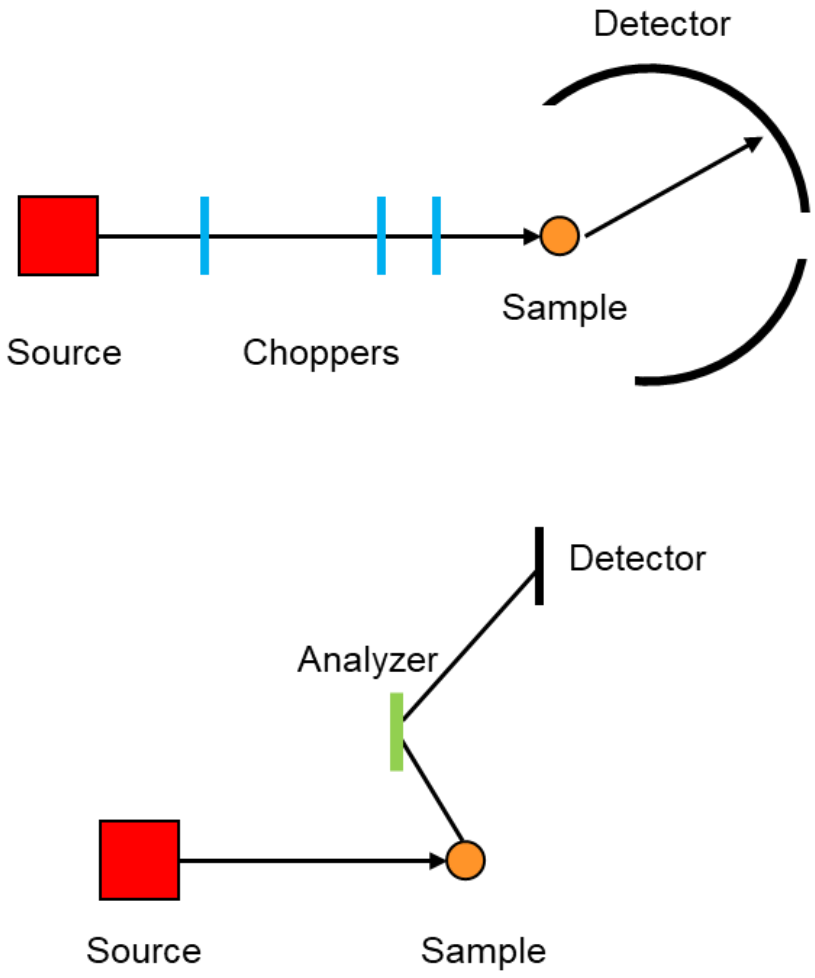

Figure 1.4 Direct geometry (Top). White neutron beam from the source filtered by Choppers before hitting the sample. Detector collect information from a wide angle. Indirect geometry (Bottom). White neutron beam hit the sample. Analyzers choose scattered neutrons with certain frequency for detection.

geometry chopper spectrometer at the Spallation Neutron Source (SNS), Oak Ridge National Laboratory (ORNL). CNCS covers the energy range from 4 to 645 cm^{-1}, meeting the needed requirements to study compounds with larger *D* values. It also provides a variety of extreme sample environments, including $T \leqslant 0.05$ K, pressure $P \geqslant 2$ GPa and a 8-T magnet, making it appropriate for studying SMMs under different conditions.[22]

Vibrational Spectrometer (VISION) at SNS[23] is an inverse geometry INS spectrometer with the highest resolution broadband in the world. As shown in **Figure 1.4 (Bottom)**, a white beam is used to interact with the sample. Scattered neutrons are selected by the analyzer to reach the detector. VISION is essentially the neutron analogue of IR and Raman spectrometers. It covers the energy range of 8 to 8000 cm^{-1} with the resolution $\frac{\Delta E}{E} < 1.5\%$ and provides a pressure cell of up to 2 GPa.[24] Cooling samples to 5 K at VISION is much faster than doing so with other instruments, making it easier and faster to collect INS data. For SMMs studies, the magnetism under variable temperatures is used to identify the magnetic peaks.

1.3 Nuclear Magnetic Resonance spectroscopy

Nuclear Magnetic Resonance (NMR) spectroscopy is extensively used in chemistry for structural and kinetic studies. NMR phenomena are interpreted as nuclei respond to an oscillating magnetic field by producing electromagnetic signals that reflect the magnetic environment of the nuclei.[25] Imbalanced spin population and non-zero spin nuclides ($I \neq 0$) are necessary in achieving NMR signals. The energy gap of nuclear spin state transition is small compared to thermal energy. The population difference of different nuclear spin states following Boltzmann distribution is only a few per million. This

population difference of the lower spin state is sufficient enough for the sensitivity of the instrument. All non-zero spin nuclei carry magnetic moments, but nuclei with integer spin also have electric quadrupole moment which leads to more complicated splitting patterns. Spin ½ nuclei are openly used in NMR since their spherical charge distribution makes spectra easier to interpret (e.g., ^{1}H, ^{13}C, ^{19}F, and ^{31}P).[26]

1.3.1 Evans method

Evans method uses NMR chemical shift difference to determine the magnetic moment of paramagnetic samples in solution. Many organometallic complexes are paramagnetic. Knowing the number of unpaired electrons in the metal ions is essential for understanding the oxidation state, geometry, and ligand field strength of the compound. If the sample is paramagnetic in solution, the magnetic field generated by unpaired electrons will change the magnetic environment of the solvent molecules, which leads to a different NMR shift from the same solvent that is not in contact with the paramagnetic sample.[27] This NMR shift difference can be used to calculate magnetic moment and number of unpaired electrons of the sample. The NMR tube contains pure solvent A (50:1 volume ratio of deuterated and protio-solvent) and a capillary containing paramagnetic sample solution (sample dissolved in solvent A). Magnetic shift difference data is obtained by collecting ^{1}H NMR of paramagnetic sample solution and pure solvent at the same time. Evans method provides a tool to determine the magnetic susceptibility in solution and supplement the solid-state SQUID data.[28] Details of the calculations will be discussed in Section 2.3.2.3.

1.3.2 Inversion recovery

NMR is a powerful tool to study molecular dynamics, such as relaxations. Longitudinal relaxation time (T_1) describes the rate of energy transfer between nuclear spin system and vibration system (lattice). For T1 relaxation to happen, the motion in the lattice must cause a fluctuating magnetic field at the site of the involved nuclear. The most common source of the local fluctuation field is the direct magnetic and electric dipole interaction. In paramagnetic substances, interaction between nuclear spin and unpaired electrons can efficiently transfer energy from spin system to lattice system, thus cause a fast relaxation. Inversion recovery (IR) is known as one of the standard methods for measuring T_1. The IR is constructed by adding a 180° pulse ahead of traditional spin echo pulse sequence (**Figure 1.5**).[29] The function of the 180° pulse is to flip the vertical magnetization to the opposite direction of the external magnetic field (B_0). During the inversion time, the flipped spins seek to re-establish equilibrium magnetization along vertical direction through T_1 relaxation. The 90° pulse changes the spins into the transverse plane. Then, the inhomogeneities local magnetic field causes spins to dephase. Shortly after, the second 180° pulse flips the entire ensemble and refocuses the spin into a spin echo. The net longitudinal magnetization is controlled by adjusting inversion time, also called delay time, in the pulse sequence. By the time the output signal is zero (*null-time*), T_1 can be calculated by **Eq. 1.5**.[30]

$$\textit{Null-time} = T_1 * \ln 2 \qquad \text{(Eq. 1.5)}$$

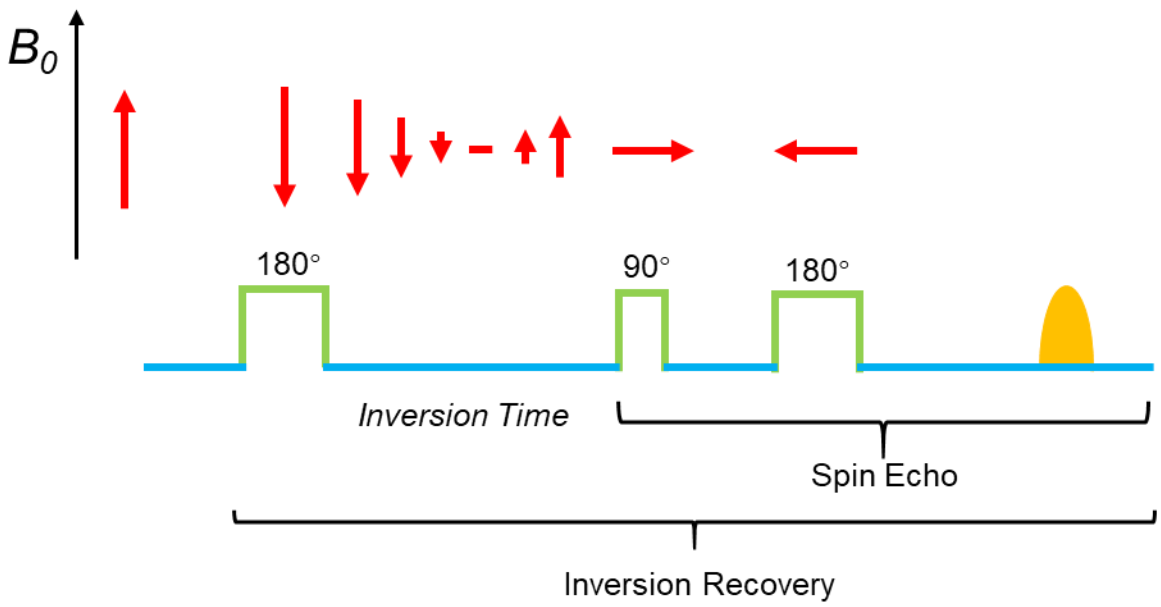

Figure 1.5 Pulse sequence of inversion recovery and spin echo. Red arrows stand for net magnetization.

2. Magnetic properties of Mn(III) porphyrin halides

2.1 Introduction

Metalloporphyrins have been actively studied due to their special biological and chemical properties. Hemoglobin, the most well-known metalloporphyrin, performs its biological functions as a paramagnetic compound. The magnetism of this protein plays a key role in oxygenation and deoxygenation.[31-34] As introduced before, ZFS is an important property to characterize the electronic and geometric status of the transition metal complexes. It describes various interactions of unpaired electrons that lead to a lifting of degenerate spin microstates. However, the origins of the ZFS are not well understood microscopically. A simple ligand field theory is not enough to explain how different coordination environments correlate to the change of the sign and magnitude of ZFS parameters in different molecules. Insights on the effect of metal-ligand interaction on ZFS could provide valuable synthetic strategies for making better SMMs.[35]

The magnetic properties of compound Mn(TPP)Cl (H_2TPP = tetraphenylporphyrin) has been studied previously by High-frequency Electron Paramagnetic Resonance (HF-EPR), magnetic susceptibility and inelastic neutron scattering (INS), yielding D = -2.3(2) cm^{-1}.[17, 36-38] Duboc and coworkers[39] have conducted a systematic theoretical study of the zero-field splitting in coordination complexes of mononuclear Mn(III) complexes. The CASSCF *ab initio* calculation of Mn(TPP)Cl gives D = -1.98 cm^{-1} which is close to the experimental value. Magnetic properties of its other halide analogs, Mn(TPP)X (X = Br **(1)**, I **(2)** and F **(3)**; **Figure 2.1**), have not been reported. Having a comparison of a series of different halide analogs is helpful for revealing the ligand effect on ZFS. The currently chapter is a discussion of experimental studies of Mn(TPP)X by HF-EPR, INS, magnetic susceptibility, and NMR spectroscopy.

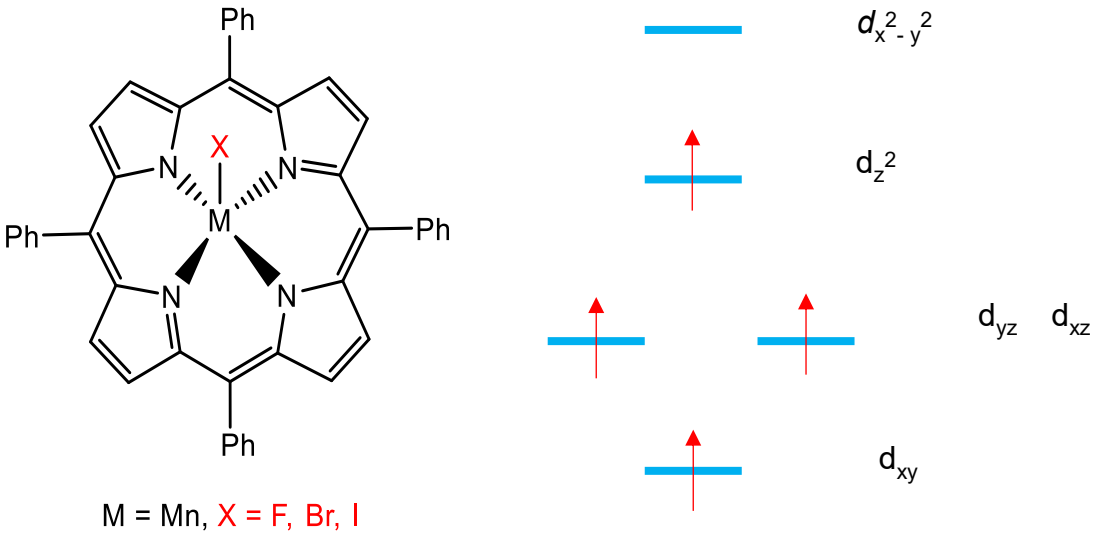

Figure 2.1 Structures (Left) and d-orbital splitting (Right) of Mn(TPP)X.

2.2 Experimental section

Samples of **1-3** were prepared by the reported method of Powell in 1984.[40] The reported crystal structure of Mn(TPP)I (monoclinic) and Mn(TPP)Br (monoclinic) were crystallized in toluene.[41] In our preparation, **1** and **2** were crystallized in chloroform ($CDCl_3$) to avoid the large incoherent neutron scattering from hydrogen. The crystal structure of **2** was solved, but the position of $CDCl_3$ was unknown. The disorder of the lattice cell may have been caused by the presence of the solvent molecules. The crystal structure of **1** could not be solved due to poor crystal quality. Unlike its halide analogs which readily form single crystals, **3** did not form single crystals in our repeated attempts. All we were able to obtain were most likely polycrystalline samples. The attempts to obtain the structure of **3** by powder X-ray diffraction, including using the intense synchrotron-radiation light source research facility at Argonne National Laboratory, were not successful. The elemental analysis of the sample was given by Complete Analysis Laboratories. The sample was dried in 90 °C oven overnight and packed under nitrogen atmosphere. Calculated: C 76.96%, H 4.11%, N 8.16%; Observed: C 75.72%, H 4.39%, N 7.77%. The difference of the C analysis is 1.24%, which is larger than the typical error of 0.40%. The UV-Vis spectra of 1-3 were taken in $CDCl_3$ (**Figure 2.2**) and matched with the published UV-Vis data.[40]

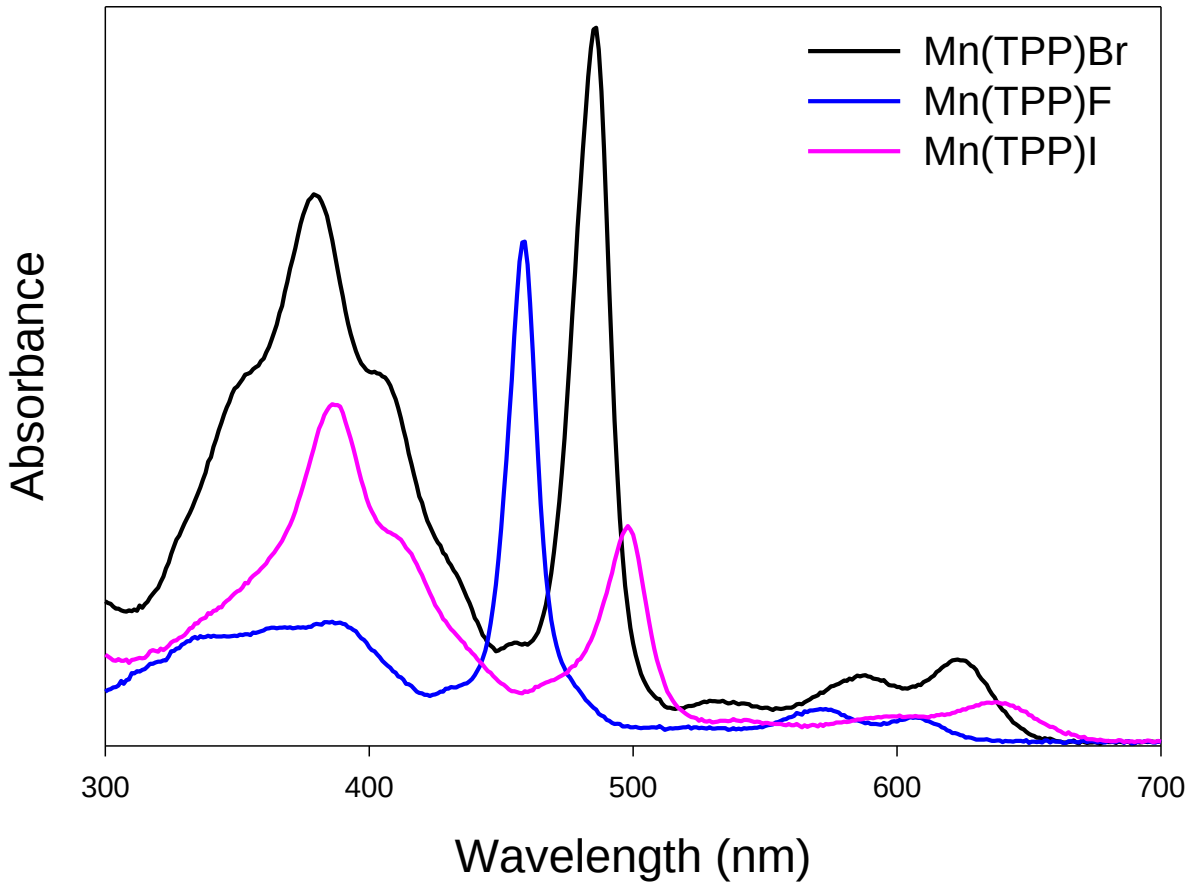

Figure 2.2 UV-Vis spectra of **1-3** in chloroform.

2.3 Results and discussion

2.3.1 Mn(TPP)X (X = Br, I)

2.3.1.1 HF-EPR

Samples of **1-2** prepared in our laboratory were sent to Dr. Jurek Krzystek of National High Magnetic Field Laboratory who, working with Prof. Joshua Telser of Roosevelt University, collected the HF-EPR spectra discussed below.

HF-EPR response of 1 represents powder spectra of an $S = 2$ spin species with moderate negative ZFS on the order of -1 cm^{-1}. **Figure 2.3 (Top)** shows a typical spectrum recorded at 10 K, and at the highest end of frequencies used, 322 GHz, along with its simulations. Two more spectra, recorded at lower frequencies, are shown in **Figures S-1** and **S-2 (Top)** in the Supplementary Information. Although the spectra show a presence of more than one species, spin Hamiltonian parameters for the dominant species could be well established using tunable-frequency EPR methodology,[42] as shown in **Figure S-3 (Top)**. Spin Hamiltonian parameters, obtained from fittings and used in the simulations, are collected in **Table 2.1**. From a visual comparison of the single-frequency spectra and the two cases of simulations for each of them, one for $D < 0$, and the other $D > 0$, it is apparent that D is *negative* in **1**.

HF-EPR response of **2** is different from that of **1**. **Figure 2.3 (Bottom)** shows a typical spectrum recorded at 10 K, and at the same frequency as the bromide analog, 322 GHz, along with its simulations. Two more spectra, recorded at lower frequencies, are shown in **Figures S-1** and **S-2 (Bottom)** in the Supplementary Information. Although the quality of the spectra is somewhat lower than that of **1**, and there is noticeable presence of a minority spin species, it is clear that the sign of D in **2** is *positive*.

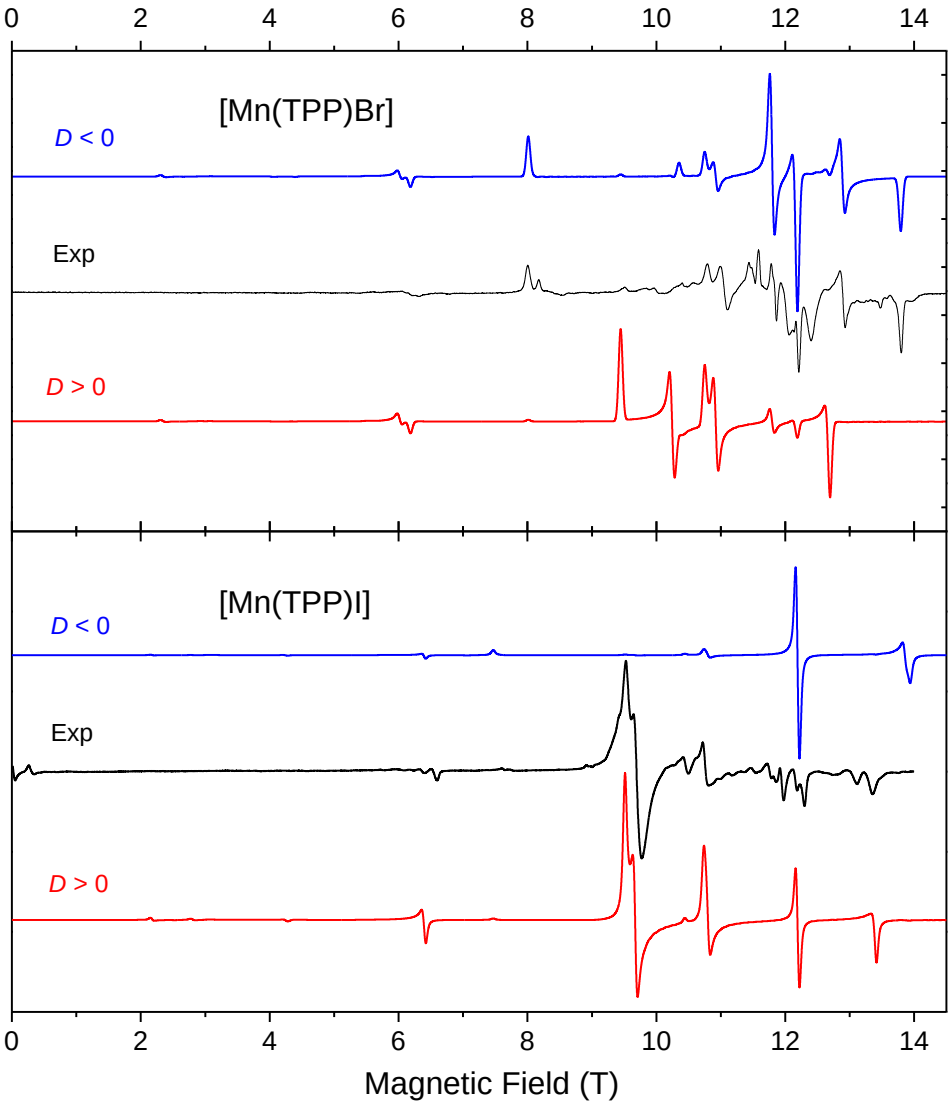

Figure 2.3 HF-EPR spectra of **1** (Top) and **2** (Bottom) at 10 K and 321.6 GHz (black traces) and their powder-pattern simulations (colored traces). The spin Hamiltonian parameters used in simulations were the same as in **Table 2.1** for **1** and slightly adjusted for **2**. Blue traces: $D < 0$; red traces: $D > 0$. Two near-zero field resonances in the **2** spectrum indicate a minority spin species with ZFS on the order of 4 cm^{-1}, typical for octahedrally-coordinated Mn(III).

Table 2.1 Parameters of Mn(TPP)X (X = Cl, Br, I)

Complex	D (cm^{-1})	E (cm^{-1})	E/D	g_x	g_y	g_z
Mn(TPP)Cl[17,43-45]	-2.290(5)	0.00(1)	0.00	2.005(5)	2.005(5)	1.98(2)
Mn(TPP)Br **(1)***	-1.091(3)	0.087(2)	0.08	1.996(4)	1.985(5)	1.994(2)
Mn(TPP)I **(2)***	+1.30(1)	0.010(5)	~0.01	1.965(5)	1.971(1)	1.930(5)

* Current HF-EPR work.

In addition, both single-frequency spectra and the 2-D field vs. frequency (energy map, **Figure S-3 (Bottom)**) show that the *g*-values in **2** (1.93–1.97) are markedly lower than 1.99–2.01 which are the usual numbers found in manganese coordination complexes at any oxidation state.

2.3.1.2 Inelastic Neutron Scattering

The INS spectra were taken at CNCS, Spallation Neutron Source, Oak Ridge National Laboratory, between 1.7 and 25 K. Powder samples were sealed in an aluminum can and fixed on the end of the sample holder before being placed inside the neutron beam. As shown in **Figure 2.4**, the intense peak at 0 cm^{-1} is the elastic band. On the right and left side of this elastic band are the inelastic scattering peaks of neutron lose and gain energy respectively. Sign and magnitude of *D* in **1** can be easily extracted from the temperature dependence of the ZFS peaks. Based on the $S = 2$ ZFS splitting diagram shown in **Figure 2.4 (Right)**, when $D < 0$, the five M_S states split into $M_S = \pm 2$ (ground state), $M_S = \pm 1$ (first excited), and $M_S = 0$ (second excited states). The energy gaps of the first and second excitation are $3D$ and D, respectively. At 1.7 K, the strong peak centered at 3.21 cm^{-1} ($3D$) on the neutron energy-losing side is due to the transition from $M_S = \pm 2$ to $M_S = \pm 1$. Transitions from $M_S = \pm 1$ to $M_S = \pm 2$ and $M_S = \pm 1$ to $M_s = 0$ are also observed at -3.21 cm^{-1} and 1.07 cm^{-1} (D) positions. They are less intense than the $M_S = \pm 2 \rightarrow M_S = \pm 1$ transition because of the low population of $M_S = \pm 1$ states at 1.7 K. The $M_S = 0 \rightarrow M_S = \pm 1$ transition is not observed at 1.7 K due to the extremely low population of the $M_S = 0$ state. With increasing temperature, $M_S = 0$ and $M_S = \pm 1$ states are getting more populated. The transitions originated from these states become stronger than at 1.7 K while

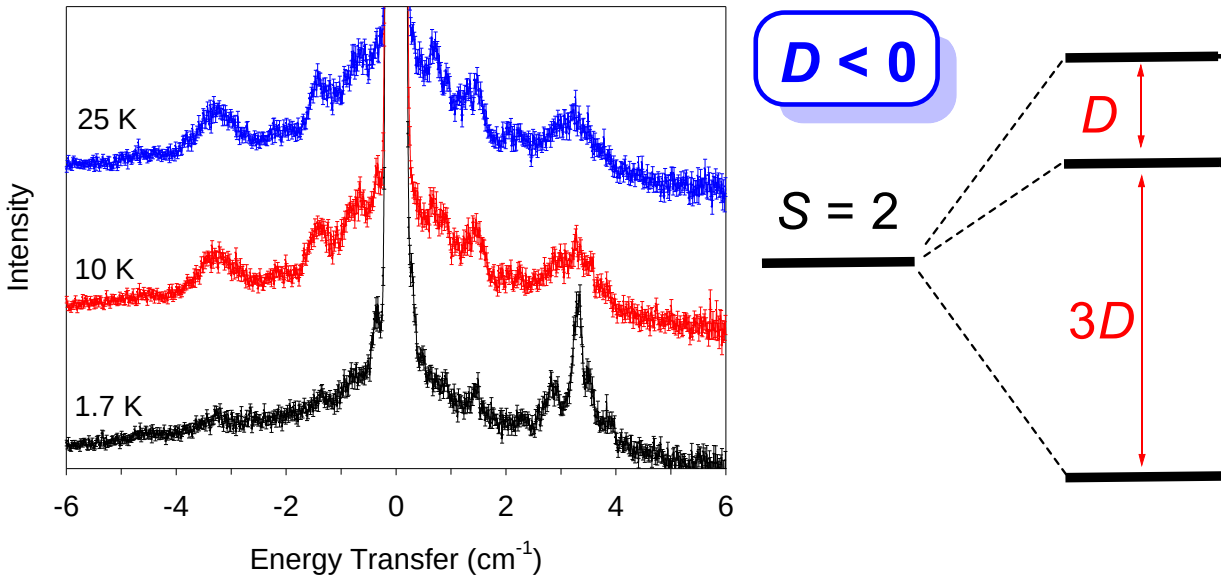

Figure 2.4 INS spectra (Left) and ZFS diagram (Right) of **1**.

the peak at 3.21 cm^{-1} becomes weaker. This temperature dependent pattern matches well with the $S = 2$, $D < 0$ ZFS splitting diagram. From the INS data, if $E = 0$, $D = -1.07$ cm^{-1}, which is close to the D value determined by HF-EPR: $D = -1.091(3)$ cm^{-1}.

The temperature dependence behavior of **2** (**Figure 2.5**) is different from that of **1**. Sign and magnitude of D can be identified from the neutron energy gain side of the spectra. Compared to the 1.7 K spectrum of **1**, which has only one weak peak at the neutron energy gain side, a peak clearly stands out at -0.90 cm^{-1} position in **2**. This implies that the first excited state of the **2** has much lower energy than that of **1**. As shown in **Figure 2.5 (Right)**, the -0.90 cm^{-1} peak corresponds to the transition from $M_S = \pm 1$ to $M_S = 0$. As temperature increases, the peak centered at -2.68 cm^{-1} starts to become more intense. This peak is assigned to the transition from $M_S = \pm 1$ to $M_S = \pm 2$. This temperature-dependent pattern matches well with the $S = 2$, $D > 0$ ZFS splitting diagram. From the INS data, $E = 0$, $D = 0.90$ cm^{-1}. This is close to the D value determined by HF-EPR: $D = 1.30$ cm^{-1}.

There are more than two peaks on both the neutron energy gain and loss side of the spectra because of the presence of traverse anisotropy (E). Although the E parameter is small for both compounds ($E = 0.087$ cm^{-1} for **1**; $E = 0.010$ cm^{-1} for **2** based on HF-EPR), it causes additional splitting of the D and $3D$ peaks which further complicates the spectra. An effort was made to simulate the INS eigenvalues for the energies of the allowed transitions for **1** and **2** with the MAGPACK program. Getting a good fit for all peaks in the INS spectra proved to be extremely difficult. Since D and E values were determined by HF-EPR, no additional attempts were made to simulate the INS spectra.

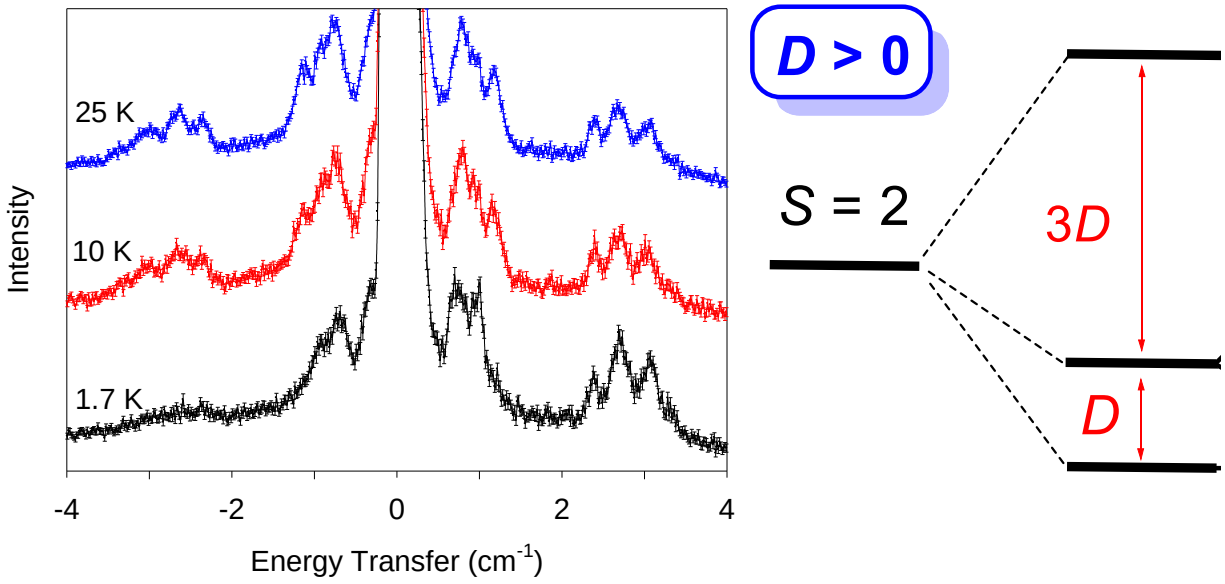

Figure 2.5 INS spectra (Left) and ZFS diagram (Right) of **2**.

It should be pointed out that a similar change of the sign of *D* parameters from a bromide to an iodide has been reported for Mn(cyclam)X_2 (X = Br and I).[46] This change is attributed to the interaction between ground state and ligand-to-metal charge transfer state. Detailed calculations are needed to support this hypothesis for our system.

2.3.2 Characterization of the magnetic properties of Mn(TPP)F

2.3.2.1 Inelastic Neutron Scattering and HF-EPR

There are no ZFS excitations in the INS data of **3** under 1.7 and 10 K. This sample for INS, prepared by a former member of the group, was later found contain NaF as shown by PXRD. Besides the INS, the rest of the data was collected with NaF-free sample. HF-EPR of the powders at 5-298 K is silent. No recognizable features from Mn(III) ion could be observed. The frozen solution EPR was measured between 5 to 10 K. Only peaks of O_2 and Mn(II) species (which are impurities) are observed.

2.3.2.2 DC susceptibility

The DC magnetic susceptibility measurement was performed at temperatures of 2–300 K using a Quantum Design superconducting interference device magnetometer with an applied field of 5000 Oe. The $\chi_M T$ value is 1.522 cm^3 K mol^{-1} at 299.975 K, which is lower than the theoretical value for one magnetically isolated high-spin d^4 Mn^{III} ion (3.0 cm^3 K mol^{-1} with S = 2 and g = 2.0). The effective magnetic moment at 299.975 K was calculated as $\mu_{eff} = \sqrt{8 * 1.522} = 3.49\ \mu_B$, suggesting there are less than 3 unpaired electrons. This effective magnetic moment is close to what reported in the literature.[47] The *d*-electron configuration of **3** cannot be simplify described by high-spin or low-spin

only. The $\chi_M T$-T curve of this compound is different from the typical isolated mononuclear Mn(III) complex.[48] Therefore, it is possible that **3** form a polymeric structure through the bridging F atoms.

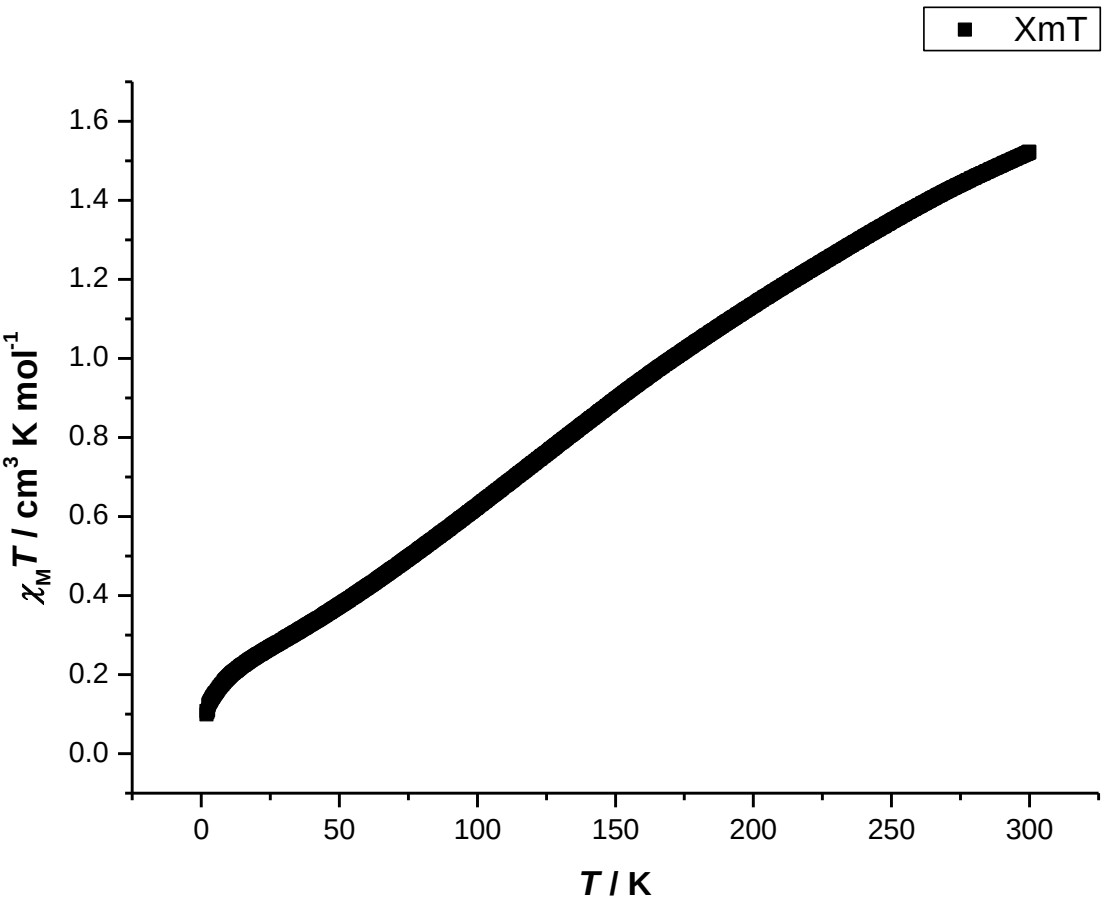

Figure 2.6 Magnetic susceptibility of **3**.

2.3.2.3 Evans method

As mentioned in the first chapter, Evans Method is a convenient way to determine the magnetic moment of the paramagnetic sample in solution. Number of unpaired electrons of the compound can be calculated based on the magnetic moment and concentration of the sample. Apparatus of the experiment is shown in **Figure 2.7**.

We prepared the mixed solvent by combining 50:1 (volume) deuterated and protio-chloroform. Solution inside the capillary was made by dissolving paramagnetic sample into the mixed solvent. Pure mixed solvent and sample solution was transferred into the NMR tube and capillary respectively. Then capillary was inserted into the NMR tube. Volume of the mixed solvent was adjusted in NMR tube until their meniscus rested at the same height. Position of the capillary was fixed by the white cap vertically. By doing so, the sample could experience an isotropic magnetic field during the measurement. Data was collected by acquiring a standard ^{1}H NMR. The featured NMR is shown in **Figure 2.8 (Left)**. The lower peak represents the chemical shift of the protio-chloroform inside the capillary, while the higher peak suggests the chemical shift of the protio-chloroform in the NMR tube. This initial chemical shift difference includes the diamagnetic effect from diamagnetic atoms in sample, solution, and apparatus. Diamagnetic effect was corrected by applying Evans method to the mixed solvent and H_2TPP-mixed solvent solution. **Figure 2.8 (Middle)** is the featured Evans method spectrum taken by placing mixed solvent in both NMR tube and capillary. Two peaks are slightly off from perfect overlapping suggests the capillary provides a small shielding effect to the sample placed inside of it. **Figure 2.8 (Right)** is the spectrum taken by placing mixed solvent and H_2TPP-mixed solvent solution into NMR tube and capillary respectively. The diamagnetic effect

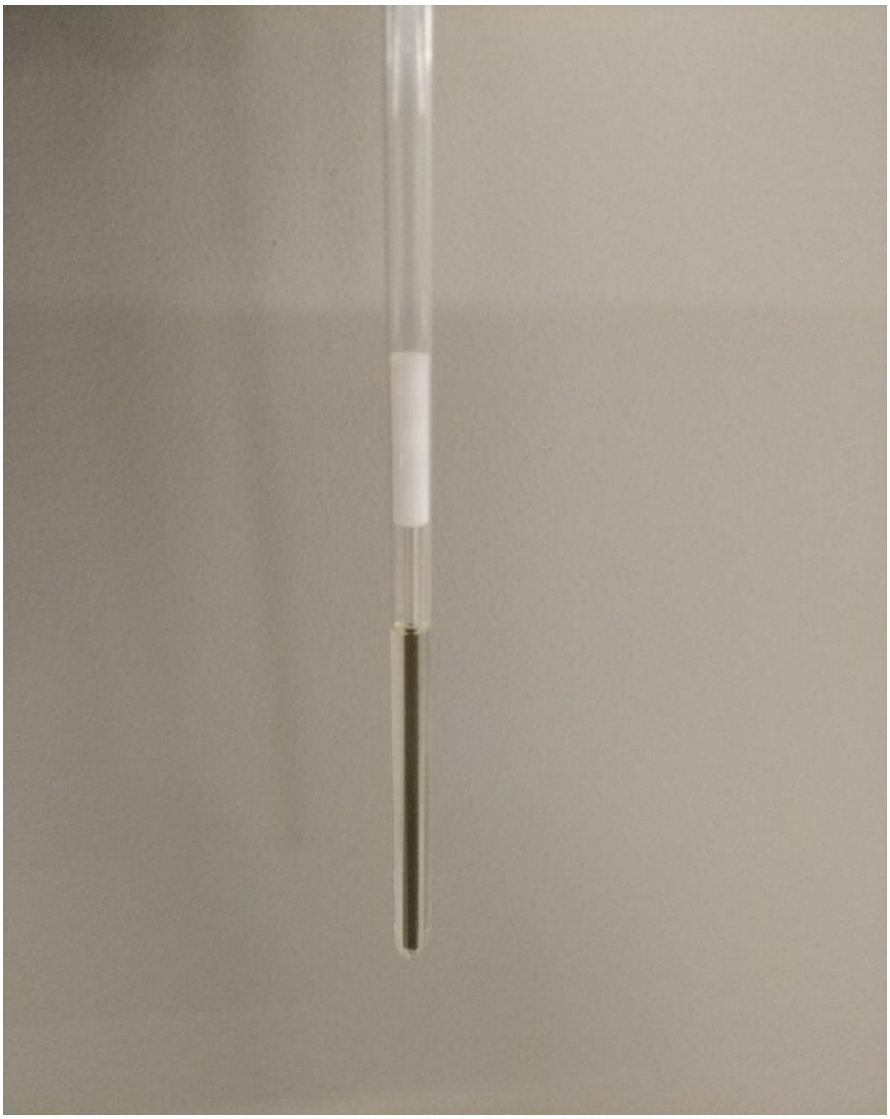

Figure 2.7 Image of the setup by the Evans method. White cap is used to secure capillary in the vertical position.

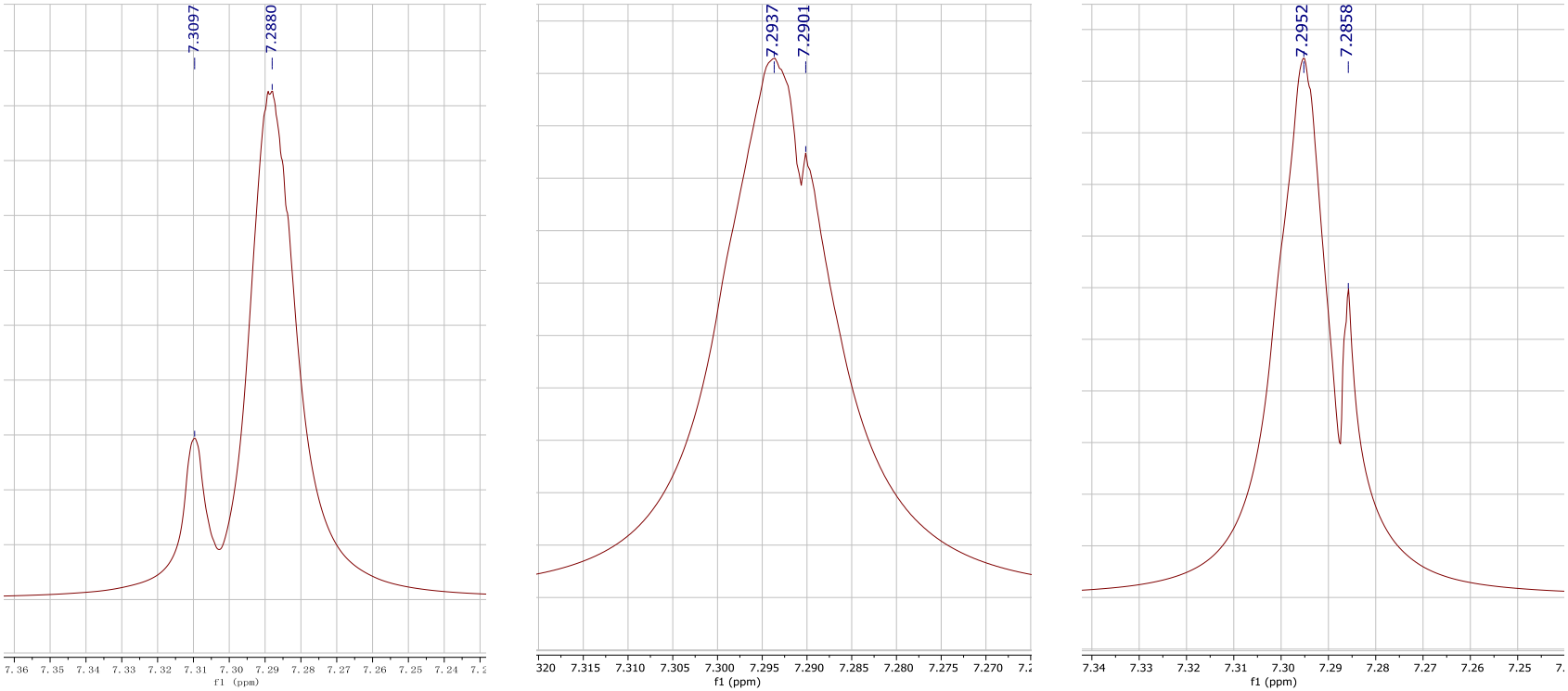

Figure 2.8 NMR spectra of **3** (Left); mixed solvent (Middle); H_2TPP (Right) by the Evans method.

of the H_2TPP solution separates two peaks further away from each other. By analyzing the diamagnetic effect from these two sources, we can estimate the corrected chemical shift difference for **3** at a certain concentration. We also measured the Mn(TPP)Cl by the same method for comparison.

Molar magnetic susceptibility X_M (cm^3/mol) can be calculated by substituting the corrected peak difference into **Eq. 2.1**.[27, 49]

$$X_M = \frac{3\Delta f}{4\pi F c} \qquad \textbf{(Eq. 2.1)}$$

where Δf is the frequency difference (Hz) between the shifted solution and the pure solvent peak, *F* is the spectrometer radiofrequency (Hz), *c* is the concentration of paramagnetic species (mol/mL).

To get the magnetic moment (μ), plug X_M into **Eq. 2.2**,

$$\mu = \sqrt{8(X_M)T} \qquad \textbf{(Eq. 2.2)}$$

where $\sqrt{8}$ comes from $[(3k_B)/N\beta^2]$, β is the Born magneton of the electron 9.3 × 10^{-20} $erg{\cdot}G^{-1}$, k_B is known as Boltzmann constant, *N* is Avogadro's number, and *T* is the temperature (K).

The magnetic moment links with number of unpaired electrons through **Eq. 2.3**.

$$\mu = g\sqrt{S(S+1)} = \sqrt{n(n+2)} \qquad \textbf{(Eq. 2.3)}$$

In this equation, we assume all of the magnetic moments come from the spin part of the unpaired electron. Since the orbital motion is, in general, small in first-row transition metals. *g* is the gyromagnetic ratio which equal to 2.00023 μ_B for free electrons, *S* is the total spin quantum number, and n is the number of unpaired electrons.

We studied the standard solution ^{1}H NMR of the **3** in $CDCl_3$. **Figure 2.9** shows a paramagnetic shifted peak at -19.47 ppm, which is consistent with the reported spectrum.[50] This implies that in solution, **3** molecules exist as monomers. The results of the Evans method experiments are listed in **Table 2.2**. The magnetic moment μ for both **3** and Mn(TPP)Cl samples solution at room temperature is close to the standard high-spin state $S = 2$ ($\mu = 4.90$) which suggests there is no additional coupling between **3** molecules in solution.

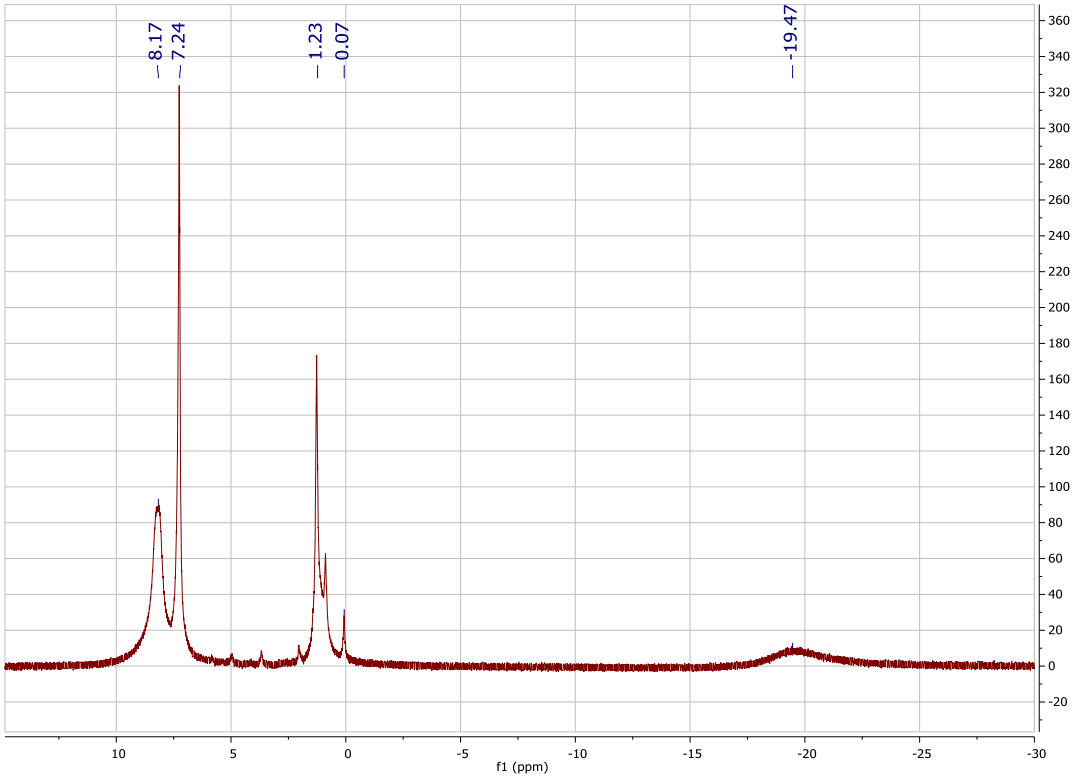

Figure 2.9 Standard ^{1}H NMR spectrum of **3** in $CDCl_3$.

2.3.2.4 Solid-state ^{13}C cross-polarization and inversion recovery NMR spectroscopy

Solid-state nuclear magnetic resonance spectroscopy (SSNMR) is a technique that can provide structural information for non-crystalline materials. Solution NMR spectra contains a series of narrow peaks because the anisotropic interactions between molecules are averaged by rapid random tumbling. Peaks in SSNMR are relatively broader than in solution even under high power proton decoupling and magic-angle spinning.[51-52] Cross-polarization (CP) is a technique that transfers the energy from the abundant proton source to a less abundant nucleus (e.g., ^{13}C) during the contact time. The signal of less abundant nucleus is detected when ^{1}H is decoupled. By running ^{13}C CP SSNMR and inversion recovery NMR experiment, we can focus on the protons that are directly connected to the aromatic carbon and ruled out the signals from impurities.

We conducted ^{13}C CP SSNMR to **3** (**Figure 2.10**), H_2TPP (**Figure 2.11**), and Mn(TPP)Cl (**Figure 2.12**) at room temperature under the spin rate of 6500 and 11500 Hz. Even though the peaks are broad, we can still estimate that they are all within the typical aromatic carbon region (120-150 ppm). Due to its paramagnetic property, the peak of Mn(TPP)Cl is the broadest among the three and shifted to higher ppm. No spinning sideband was observed for Mn(TPP)Cl even when under the spin rate of 11500 Hz. Surprisingly, the peak broadening feature of **3** behaves more like diamagnetic H_2TPP instead of the other paramagnetic compound Mn(TPP)Cl. Spinning sidebands of both **3** and H_2TPP are clearly showed up at 6500 Hz and pushed further apart when increasing spin rate to 11500 Hz.

Table 2.2 Experiment details using the Evans method and results of Mn(TPP)F (**3**; Experimental Nos. 1-3) and Mn(TPP)Cl (Experimental Nos. 4-5)

Experiment No.	Peak shift		Mass (10^{-4} g)	Volume (mL)	Concentration (10^{-4} mol/L)	Magnetic moment μ
	ppm	Hz				
1	0.0335	20.1	9.4	1.5	9.126	4.96
2	0.0241	14.5	14.1	3.0	6.845	4.95
3	0.0210	12.6	15.8	3.5	6.574	4.77
4	0.0379	22.74	23.5	3.0	11.14	4.76
5	0.0191	11.46	13.2	3.0	6.258	4.70

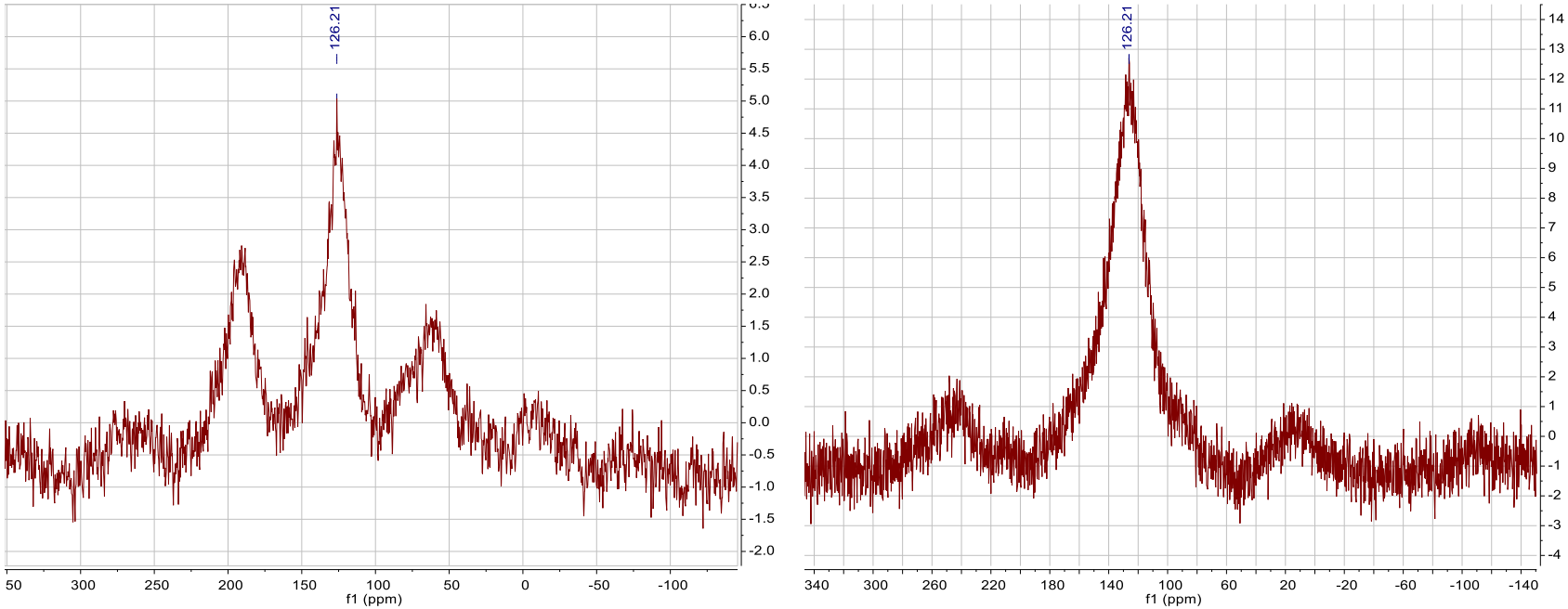

Figure 2.10 Solid-state ^{13}C NMR spectra of **3** with a spin rate of 6500 Hz (Left) and 11500 Hz (Right) at 296 K.

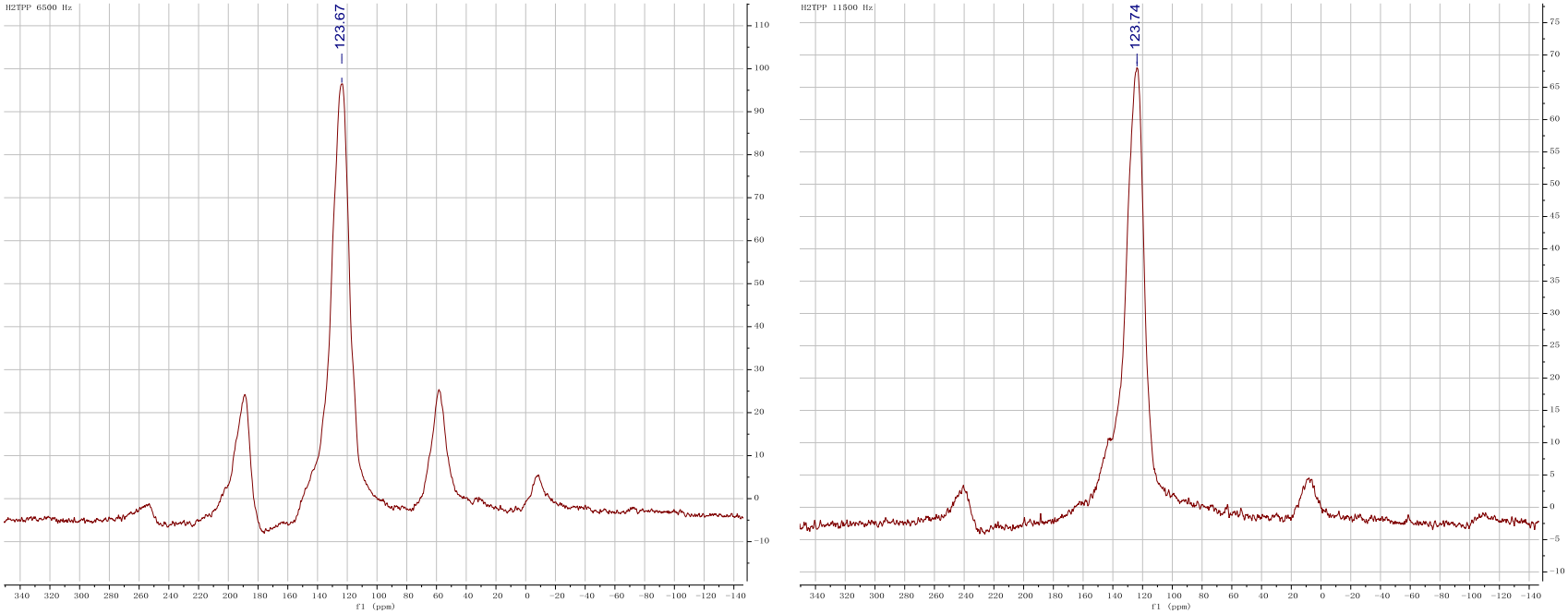

Figure 2.11 Solid-state ^{13}C NMR spectra of H_2TPP with a spin rate of 6500 Hz (Left) and 11500 Hz (Right) at 296 K.

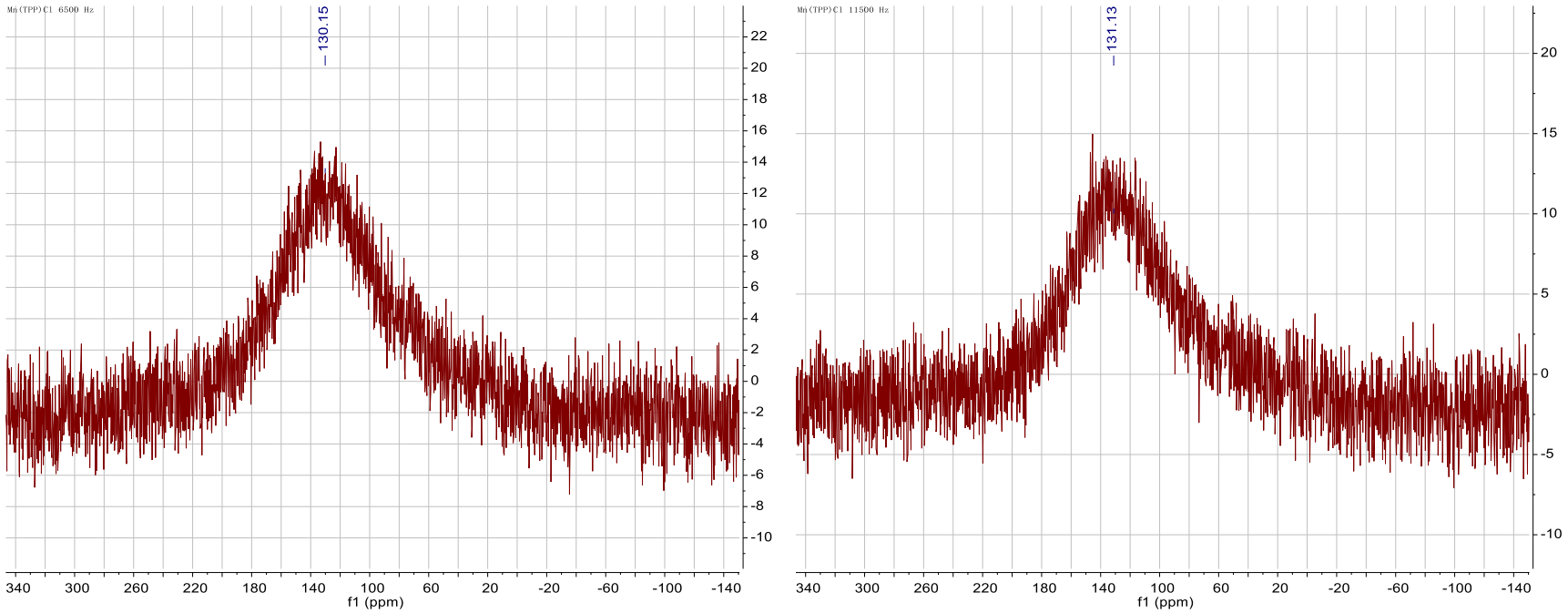

Figure 2.12 Solid-state ^{13}C NMR spectra of Mn(TPP)Cl with a spin rate of 6500 Hz (Left) and 11500 Hz (Right) at 296 K.

The inversion recovery experiment provides information about spin-lattice relaxation time (T_1) of the nucleus. Inversion recovery experiment was repeated for different delay values. ^{13}C cross-polarization (CP) is applied to measure T_1 of H atoms. As shown in **Figures 2.13** and **2.14**, when the delay time is long enough, we can obtain the same spectra as a regular solid-state ^{1}H NMR. As decay time decreases, phase of the spectra starts to become inversed. By the time the signal completely vanishes, the delay time is called *null-point*. As mentioned in Chapter 1, the rough T_1 value can be estimated from the *null-point* as **Eq. 2.5**. As shown in **Figures 2.13 and 2.14**, the *null-point* of **3** and H_2TPP are found to be 5 ms and 2 s respectively. Thus, T_1 of **3** (7.2 ms) is about 400 times faster than TPP (2.9 s). This strong evidence shows that **3** is paramagnetic under this condition. We have also tried to run Mn(TPP)Cl for comparison. However, the CP signal of Mn(TPP)Cl was too broad to run inversion recovery.

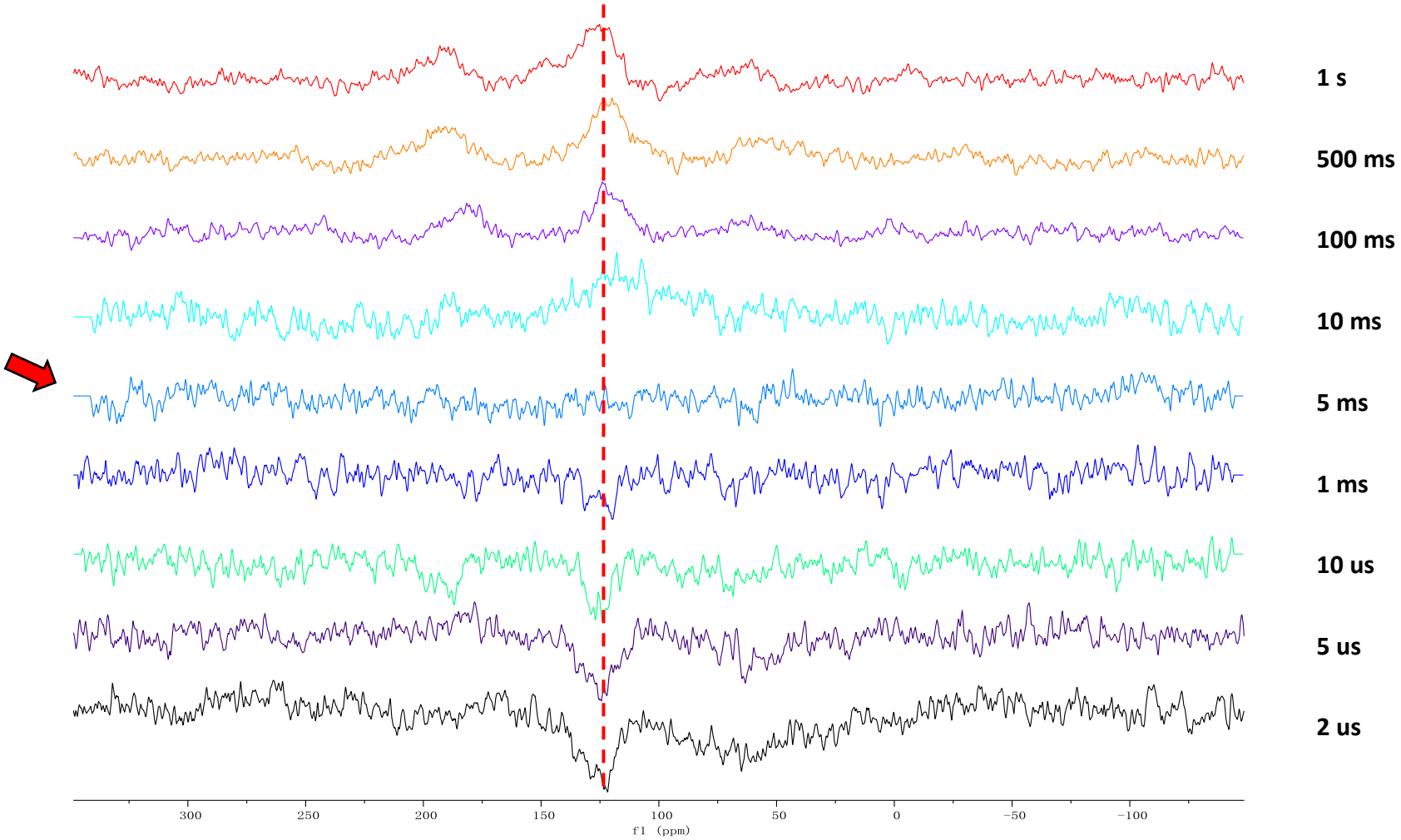

Figure 2.13 ^{13}C cross-polarization inversion recovery spectra of **3**. Red arrow points to the spectrum at *null-point*. Red dash line shows the featured peaks.

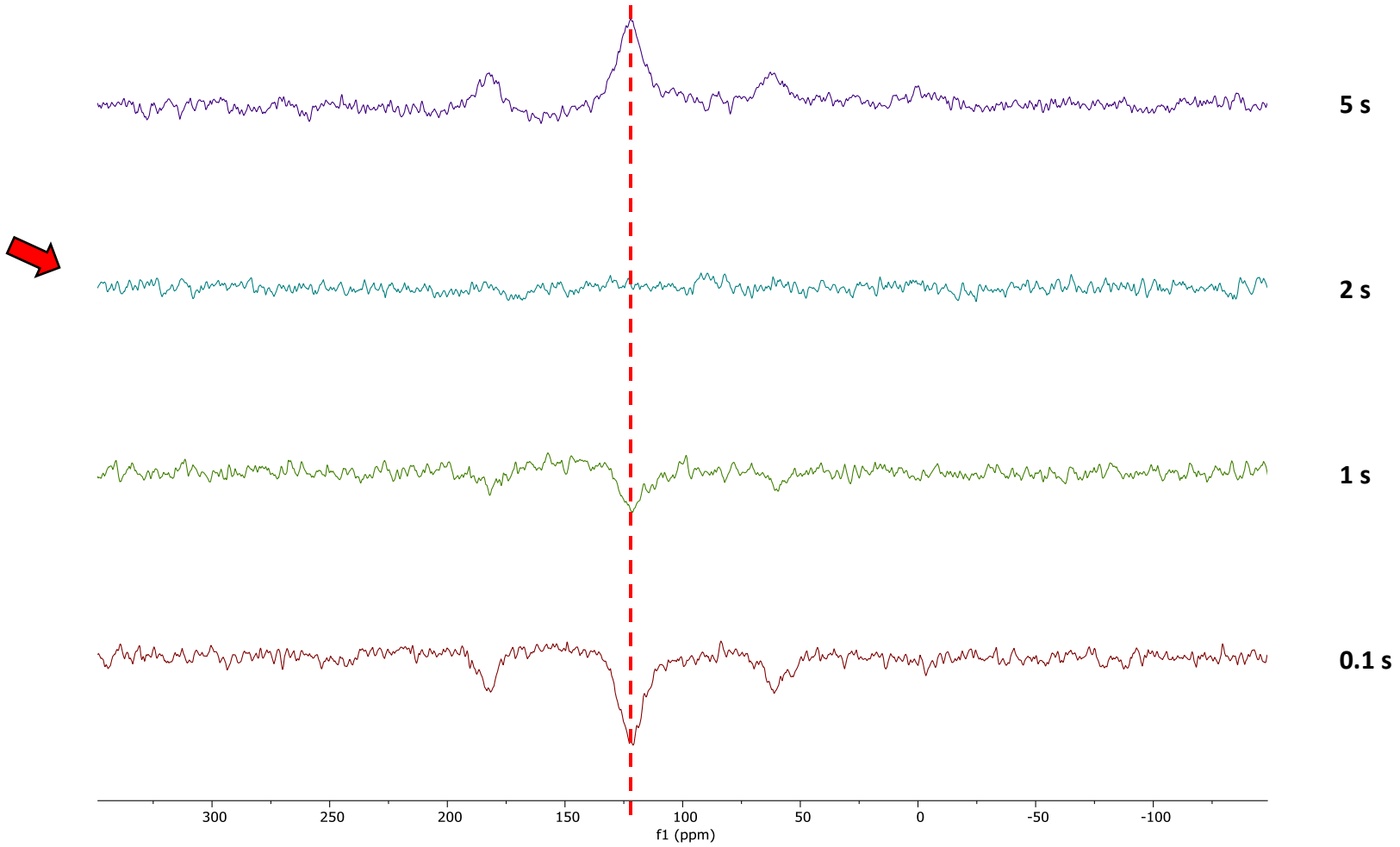

Figure 2.14 ^{13}C cross-polarization inversion recovery spectra of H_2TPP. Red arrow points to the spectrum at *null-point*. Red dash line shows the featured peaks.

2.4 Conclusion

A series of manganese porphyrin complexes with different halides Mn(TPP)X [H_2TPP = tetraphenylporphyrin; X = Br **(1)**, I **(2)** and F **(3)**] were prepared and studied by INS, HF-EPR, DC susceptibility and NMR spectroscopy. The sign and magnitude of *D* were revealed by INS and HF-EPR. HF-EPR spectra give $D = -1.09\ cm^{-1}$, $E = 0.087\ cm^{-1}$ for **1** and $D = +1.30\ cm^{-1}$, $E = 0.010\ cm^{-1}$ for **2** at low temperature. **3** is EPR silent in both solid (5-290 K) and frozen solution (10 K in chloroform) state, making it different from its Br and I analogies. No ZFS transition was observed on INS either. Evans method was applied for measuring the magnetic moment of **3** and Mn(TPP)Cl at room temperature. It turns out that these two compounds share similar magnetic properties under this condition. It is notable that the room temperature solid-state ^{13}C NMR spectrum of **3** behaves more like a diamagnetic compound rather than paramagnetic. The DC susceptibility of **3** is different from an expected isolated mononuclear Mn(III) complex, which implies the molecules may form dimer or 1-D polymer chain through the bridging F atoms. Pedersen's review summarized a couple of low-dimensional F bridged compounds.[53] We speculate that **3** forms near perfect linear 1-D polymer with F-Mn-F angle close to 180° due to the interaction of porphyrin rings, as Birk and Čižmár have reported.[54-55] More data need to be collected to support this hypothesis.

3. Ligands effects on the magnetic anisotropy of tetrahedral cobalt SMMs $Co(EPh_3)_2X_2$ by INS

3.1 Introduction

The field of SMMs has experienced rapid progression in the last few years. Since SMM was first discovered in 1993, the record of blocking temperature (T_B), which is the maximum temperature limit to observe the magnetic hysteresis, has been improved from 4 to 60 K by 2017.[4, 56-58] Recently, Layfield[6] reported a Dy-based SMM that exhibits magnetic hysteresis at 80 K. This was the first reported SMM with T_B above the liquid nitrogen boiling temperature, which is a milestone in the development of practical high-density information storage material.

Large magnetic anisotropy is desired for SMMs to enhance its performance. Attempts have been made to improve the anisotropy. These include tuning spin-orbit coupling, zero-field splitting, symmetry and ligand field strength. Some previous experimental and theoretical studies have shown that the heavy donor atom of the ligands increase magnetic anisotropy of the first-row metals due to their larger spin-orbit coupling effect.[59-61] For example, Long[62] and co-workers reported a study of tetrahedral $(Ph_4P)_2[Co(EPh)_4]^{2-}$ (E = O, S and Se) SMMs by magnetic susceptibility and yielded D = -11, -62 and -83 cm^{-1} respectively. A similar trend was also observed in a series of octahedral Cr^{III} complexes $[Cr(dmpe)_2(CN)X]^+$ (X = Cl, Br, and I) as the magnitude of D gradually increases from Cl to I analogous.[60] A series of pseudo-tetrahedral Co^{II} complexes $Co(EPh_3)_2X_2$ [E = P, X = Cl **(4)**, Br **(5)**, I **(6)**; E = As, X = I **(7) Figure 3.1 (Left)**] with large magnetic anisotropy have been reported recently.[63-66] The anisotropy barrier ($2D$) for **6** (-73.8 cm^{-1}) is much larger than those of its lighter halide analogs **4** (-23.2 cm^{-1}) and **5** (-25.0 cm^{-1})**.** The values of $2D$ for **7** (-149.4 cm^{-1}) is much larger than its phosphine analog **6**. **4** is studied by HF-EPR, while **5**, **6**, and **7** were measured by

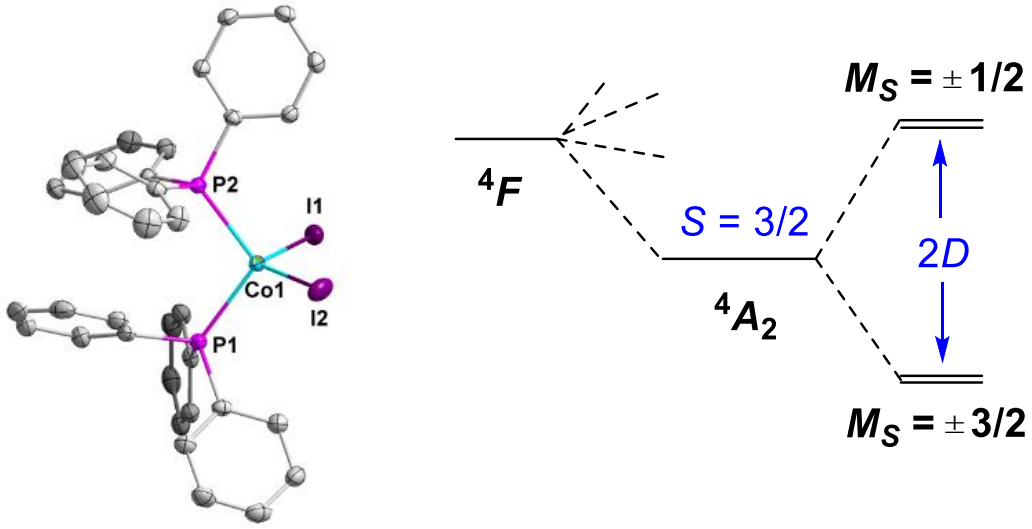

Figure 3.1 Molecular structure of **6**. Compounds **4-7** share a similar structure (Left). Hydrogen atoms are omitted for clarity. Low-lying energy levels in high-spin, 4-coordinated, C_{2v}, d^7 complexes (Right).

magnetic susceptibility. It is rare to see halides substitution introduce such dramatic changes to the anisotropy barrier. In this work, we probed their anisotropy barrier by variable-temperature and variable-magnetic field INS.

3.2 Experimental section

Samples **4-7** were prepared by the reported method of literature.[63-65] In this work, the variable temperature INS spectra are collected by Vibrational Spectrometer (VISION) at Spallation Neutron Source, Oak Ridge National Laboratory. For each measurement, approximately 0.2 g of the powder sample was sealed in an aluminum can. The aluminum can was then fixed on the end of the sample holder and placed inside the neutron beam. VISION has two detector banks providing data for low |$\boldsymbol{Q}$| and high |$\boldsymbol{Q}$| scattering. Variable-field INS data was collected at Dick Chopper Spectrometer (DCS) at NIST Center for Neutron Research (NCNR). To determine the magnetic anisotropy barrier of **7**, 6 g of the powder sample was sealed in the aluminum can and placed into neutron beam. Sample was cooled down to 1.5-1.6 K and measured at 0, 5, and 10 T fields. The 0 T data was collected with incident neutron energy E_i = 1.81 Å, while the 5 and 10 T data were collected with E_i = 2.4 Å. With the presence of magnet inside the sample environment, the detector efficiency was reduced by about 30% in comparison to the normal environment. Therefore, when the magnetic field is on, we reduce the incident neutron energy from 1.81 Å to 2.4 Å in order to obtain a better resolution. Powder sample **4** (2 g) was measured at 0 T with E_i = 3 Å and 10 T with E_i = 3.5 Å in order to compare the results of variable temperature and variable magnetic field INS. All data were processed on DAVE.[67]

3.3 Results and discussion

3.3.1 Variable-temperature INS

Variable temperature INS has been used to distinguish magnetic and phonon excitations in single ion magnets. For example, Boskovic[68] has reported the probing of lowest-lying crystal-field splitting of deuterated Ho(III) and Er(III) complexes on PELICAN spectrometer, Australian Nuclear Science and Technology Organization (ANSTO). Different temperature dependence between magnetic and vibrational originated peaks provides direct information of excitations from different energy states. Magnetic excitation of Co(II)-Y(III) dimer SMM is measured by Brechin[69] group at LET time-of-flight spectrometer, ISIS spallation neutron source. A clear transition between two Kramers doublets is observed after Bose-correction.

Based on the magnetic form factor, the magnetic excitation should be more pronounced at low $|\boldsymbol{Q}|$, which is forward scattering in VISION. The measurements were conducted at different temperature between 5 and 100 K. **Figure 3.2** are Bose-corrected forward scattering spectra for four samples. Base on the S = 3/2 ZFS energy diagram shown in **Figure 3.1 (Right)**, the ground state term symbol is $^4A_2$, and the degenerated M_S states were lifted by ZFS with a gap of 2D. Thus, only one magnetic transition should be observed for each compound if we ignore E. As mentioned on Chapter 1, after Bose-correction, the intensity of magnetic peak should decrease with increasing temperature while the intensity of phonon peaks stays the same. Magnetic transition of **4**-**6** can be clearly observed at 29.5 cm^{-1}, 27.5 cm^{-1} and 27.3 cm^{-1} respectively because of the greatest intensity drop. However, the magnetic peak of **7** is not as apparent as the other

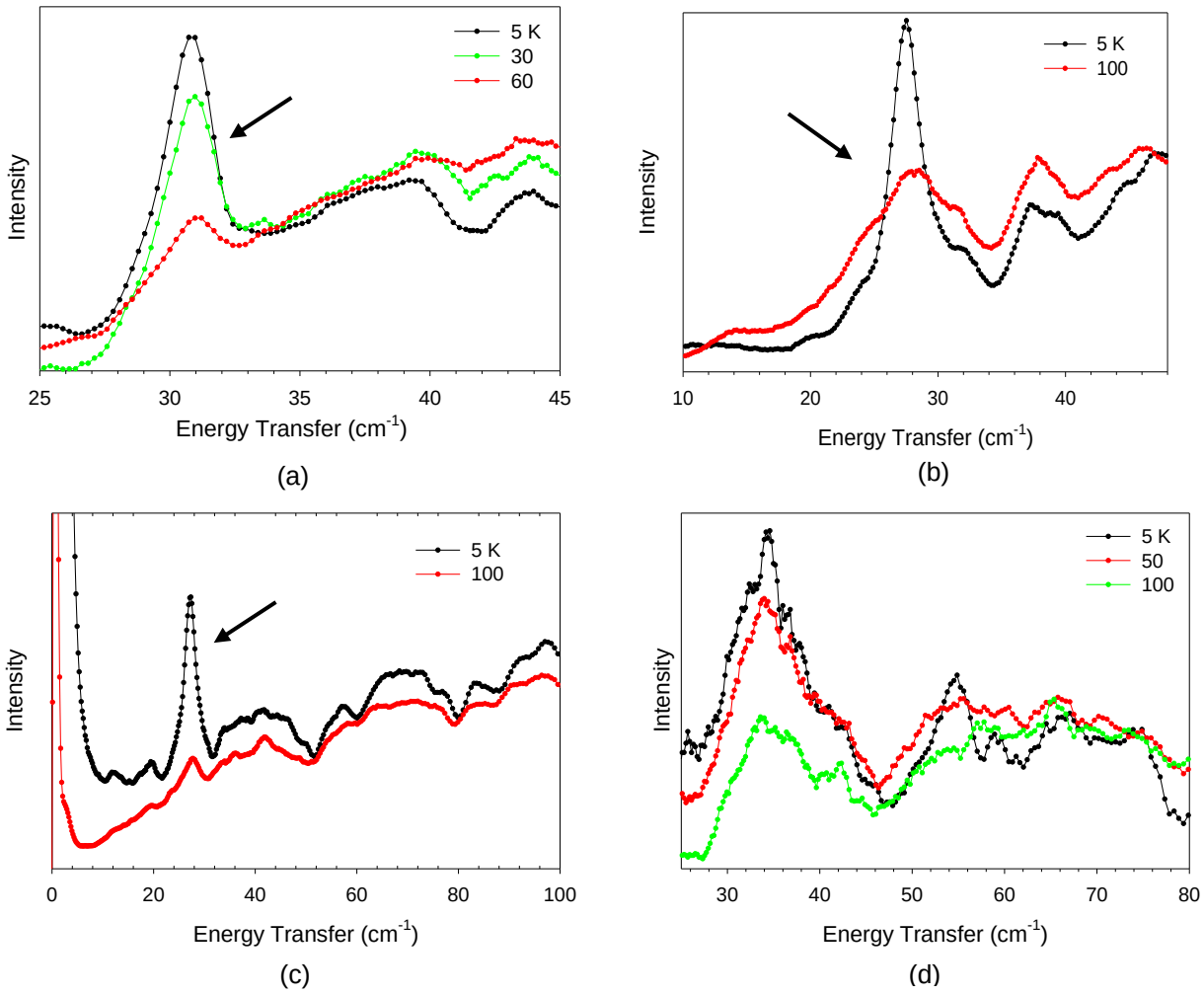

Figure 3.2 Bose-corrected forward scattering spectrum for (a) $Co(PPh_3)_2Cl_2$ (**4**), (b) $Co(PPh_3)_2Br_2$ (**5**), (c) $Co(PPh_3)_2I_2$ (**6**) and (d) $Co(AsPh_3)_2I_2$ (**7**).

three. The intensity of all the peaks changes equally. Based on the reported susceptibility data, 2*D* of **7** is much larger than that of **4**-**6**. We suspect that the magnetic peak of **7** falls into a region where the vibrational density of states is large. The relatively small intensity change of the magnetic peak may be overwhelmed by strong phonon peaks. To address this issue, we studied **7** by variable magnetic field INS.

3.3.2 Variable-magnetic-field INS

The single-to-noise ratio of the peaks are low in the DCS spectra, because the magnet blocked a large portion of the detector. Even then, the result is still very convincing. As shown in **Figure 3.3 (Left)**, the strong peak at 53.2 cm^{-1} is caused by the overlapping of phonon and magnetic peak. As the magnetic field increased, the magnetic peak shifts to higher energy due to the Zeeman effect and phonons remaining at the same position. At 5 T, the magnetic peak shows up at 61.5 cm^{-1} and the intensity of peak at 53.2 cm^{-1} was reduced. As the magnetic field increased to 10 T, the magnetic peak shifts further left to 67.3 cm^{-1} and leaves a phonon peak at 61.5 cm^{-1}. The phonon peak at 35.6, 41.7 and 74.9 cm^{-1} stayed at the same position with changing magnetic field. This peak shifting pattern indicates that the magnetic peak is located at 53.2 cm^{-1} at 0 T. Similar pattern was also observed in sample **4**. The magnetic peak at 29.6 cm^{-1} at 0 T moves away when the field was increased to 10 T. Its anisotropy barrier is consistent with what we observed at VISON.

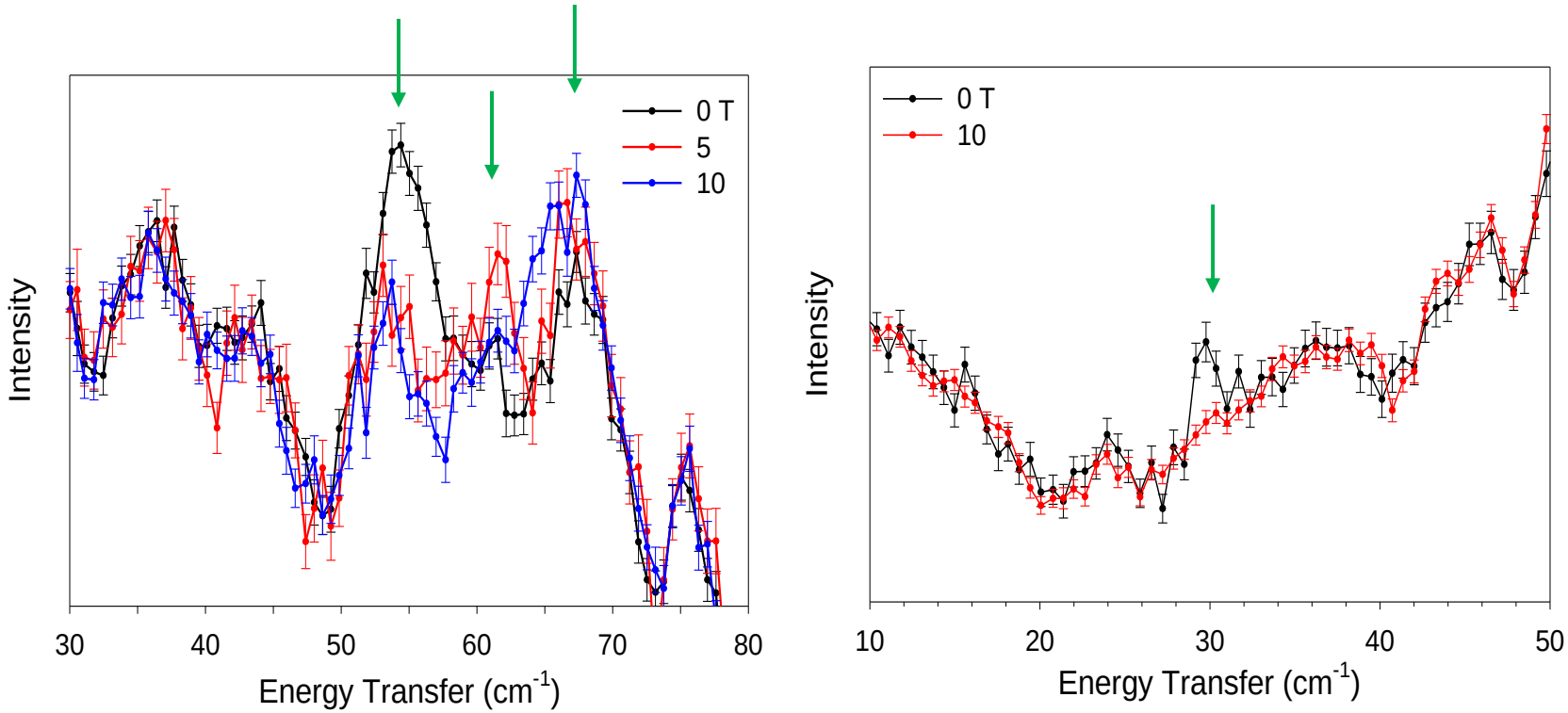

Figure 3.3 Variable-field INS data for **7** (Left) and **4** (Right).

3.4 Conclusion and future work

A summary of the peaks is given on **Table 3.1**. As we can see, due to its nature of multi-parameter fitting, the magnetic susceptibility data is not always accurate in determining *D* value. Inelastic neutron scattering provides opportunities to directly probe the anisotropy barrier. In this pseudo-tetrahedral Co^{II} system, the anisotropy barriers do not change notably when the coordinating halide ligands change from lighter Cl to heaver Br and I. However, a significant increase in the 2*D* value happens when substituting phosphine with arsine. Some calculation work should be helpful to reveal the reason behind this big magnetic anisotropy difference between P and As analogies. I speculate that this change is related to the crystal structure. The bond angle of these four complexes varies from one to another, but the average Co-E bond length of **7** (2.4982 Å) is significantly larger than that of **4** (2.384 Å), **5** (2.385 Å), and **6** (2.401 Å). This could be one perspective to consider in the future study. This work shows that INS provides accurate determination of magnetic separations in SMMs.

Table 3.1 Summary of reported (susceptibility fitting) and INS 2*D* values

Compound	ZFS (cm^{-1}) by Susceptibility	| ZFS | (cm^{-1}) by INS	Difference
$Co(PPh_3)_2Cl_2$ **(4)**	-23.2	29.5	24%
$Co(PPh_3)_2Br_2$ **(5)**	-25.0	27.5	9%
$Co(PPh_3)_2I_2$ **(6)**	-73.8	27.3	170%
$Co(AsPh_3)_2I_2$ **(7)**	-149.4	53.2	181%

4. Variable-temperature NMR study of group 10 metal complexes with macrocyclic amine N-heterocyclic carbene ligands

This work was published as:

Taotao Lu, Zhiming Liu, Carlos A. Steren, Fan Fei, Tabitha M. Cook, Xue-Tai Chen, and Zi-Ling Xue, Synthesis, structural characterization and NMR studies of group 10 metal complexes with macrocyclic amine *N*-heterocyclic carbene ligands. *Dalton Trans.* **2018**, 47, 4282.

https://pubs.rsc.org/en/content/articlelanding/2018/dt/c7dt04666a#!divAbstract

4.1 Introduction

In early 1960s, researchers believed that carbenes were too reactive to be separated.[70] However, about 30 years later, in 1991, Arduengo[71] reported the synthesis and isolation of the first stable N-heterocyclic carbene (NHC). Ever since that happened, different derivatives of NHCs and their metal complexes have become an active field in transition metal coordination chemistry. Due to their tunable steric and electronic properties, NHCs have a bright potential in catalysis, material, and medicines fields.[72-77] NHCs can be functionalized with other donor groups to give different types of polydentate macrocyclic ligands. Compared to analogous of acyclic ligands, complexes with macrocyclic effect show much higher stability.[78] Tetradentate macrocyclic NHC ligands, which share a similar structure as porphyrins, have drawn considerable research attentions. The first silver(I) tetradentate macrocyclic NHC was reported by Youngs[79] and co-workers in 2001. In this ligand, two pyridines are linked by two NHCs to form a macrocycle. Afterwards, the ligand field and magnetic properties of many NHC cyclophanes derivatives with other transition metals were studied by different groups.[80-81] In 2010, Hahn[82] reported a platinum(II) complex with macrocycle of two phosphines linked by two NHC units. In 2016, Kuhn investigated the reactivity of the oxygen molecule with heme analogue iron(II) compound, which contains four NHC units.[83]

The synthesis and application of saturated polyamine macrocyclic ligands have been extensively studied. However, the combination of secondary amine and NHC groups might lead to attractive properties. The dynamic of the ring twisting process of macrocyclic ligands with ring size over five have been known for a long time.[84] The metal complexes

with fused polydentate macrocyclic NHC ligand are expected to have the similar behavior. In this work, two ligand precursors $[H_2L^1][PF_6]_2$ and $[H_2L^2][PF_6]_2$ (**Figure 4.1**) have been made and applied to prepare **8**-**14** (**Figure 4.2**) different metal complexes. Their dynamic properties were examined by NMR spectroscopy.

4.2 Experimental section

Samples of $[ML][PF_6]_2$ [L = L^1, M = Ni (**8**), Pd (**9**), Pt (**10**); L = L^2, M = Ni (**11**), Pd (**12**), Pt (**13**)] and [Pt(L^2)(acac)] (**14**) were prepared by Prof. Xue-Tai Chen's group at Nanjing University. This author helped collect the 2-D and variable-temperature NMR spectra of **8-14** and analyze the spectra.

The 1-D and 2-D NMR spectra of **8-14** at 295 K and **8** at 318 K were recorded on a Varian VNMRS 600 MHz spectrometer at the University of Tennessee equipped with an HCN cold probe. The NMR experiments at 253 K on **8** were performed on a Varian 500 MHz spectrometer equipped with an OneNMR probe at UT. VT NMR spectra were acquired on a Bruker Avance 400 MHz spectrometer equipped with a Broad Band Inverse (BBI) probe at UT.

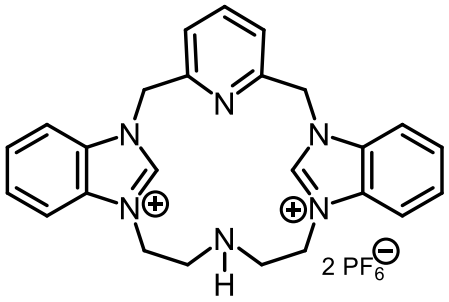

$[H_2L^1][PF_6]_2$

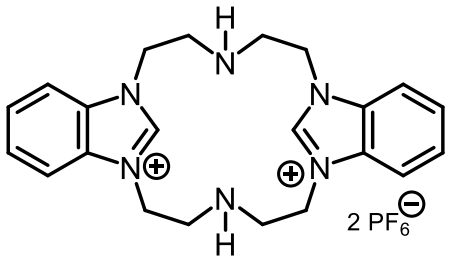

$[H_2L^2][PF_6]_2$

Figure 4.1 Ligand precursors $[H_2L^1][PF_6]_2$ and $[H_2L^2][PF_6]_2$.

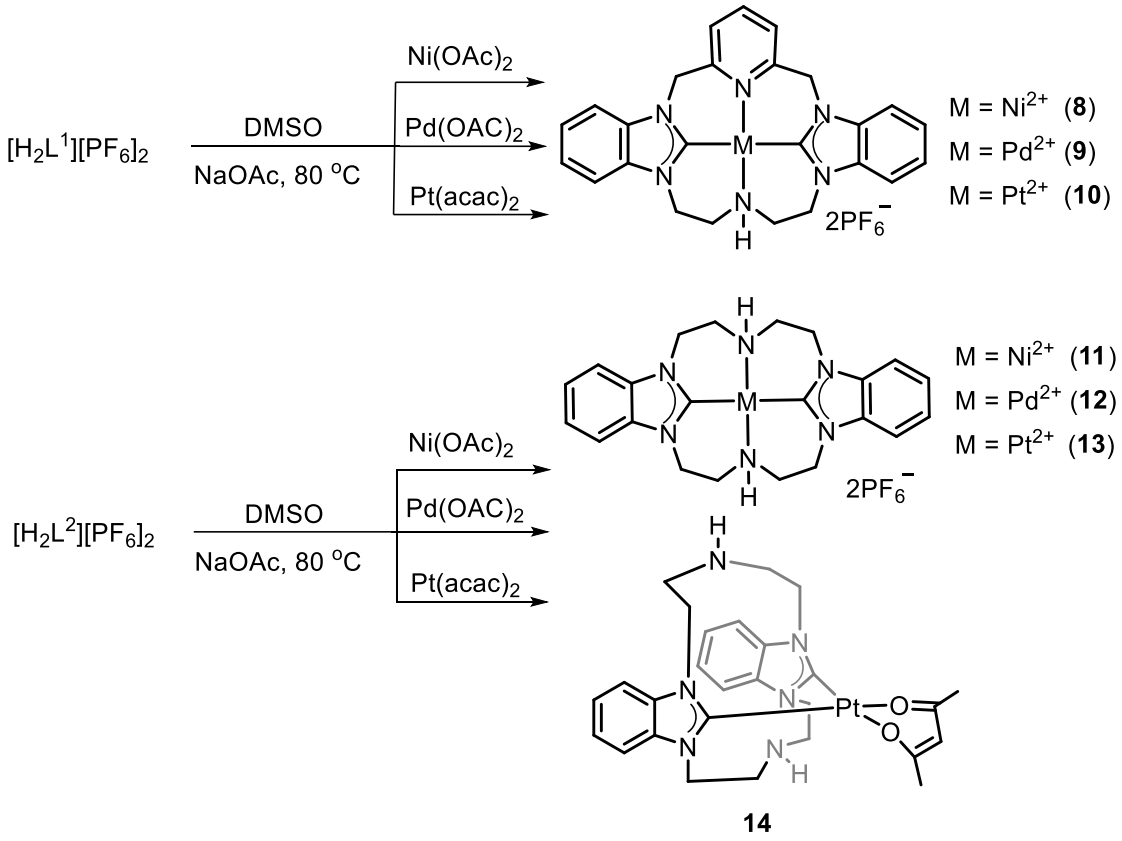

Figure 4.2 Preparation of complexes **8**-**14**

4.3 Results and discussion

VT ^{1}H NMR spectra of **8**-**14** were collected from 185 to 295 K in deuterated acetone. The ring twisting behavior was observed from two atropisomers of **8**-**10**. However, similar behavior was not observed in **11**-**13**, which suggests their dynamics are out of the NMR timescale. As shown in the crystal structures of **8**-**10** (**Figure 4.3**), the ethylene linkers between the secondary amine and benzimidazolium are on the different side of the plane, one twisted up and the other one is down. This twist causes the amine proton to be closer to one side of the ethylene but far away from the other. Therefore, protons on two ethylene linkers are magnetically inequivalent. The VT ^{1}H NMR spectra of **8** is shown in **Figure 4.4**. At 295 K, the peak at 6.23 ppm comes from the methylene between benzimidazolylidene and pyridine. The peak at 5.28 ppm corresponds to the proton on the secondary amine. Peaks at 4.93, 4.62, and 3.54 ppm are assigned to the protons of ethylene linkers. The strong peak at 2.92 ppm is due to the residual water. ^{13}C gCOSY and ^{13}C gHSQCAD conducted at 253 K were used to help assign the peaks.

The peak at 6.23 ppm gets broader with decreasing temperature and reaches decoalescence at 270 K. When the temperature decreases further, this peak splits into two multiplets. This is due to the exchanging of axial and equatorial diastereotopic protons of the methylene group. As shown in **Figure 4.5**, the chemical environment of the methylene group protons is not affected by the orientation of amine proton due to the distance, which means the chemical shift of H^1 is identical with H^3 and H^2 is identical with H^4. Therefore, the ring twisting dynamics causes the exchange between H^1 and H^2 and leaves a broadened peak at 6.23 ppm at 295 K. The vibrational barrier of **8** is calculated to be $\Delta G^{\ddagger}$ = 12.6 kcal mol^{-1}.[85] Similar behavior is also observed on the peak at 4.62 ppm

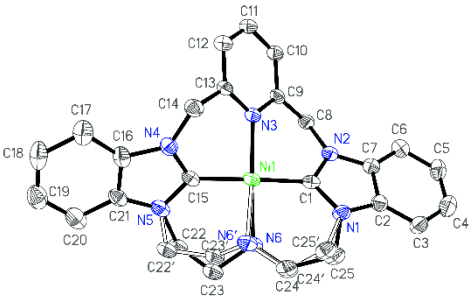

8

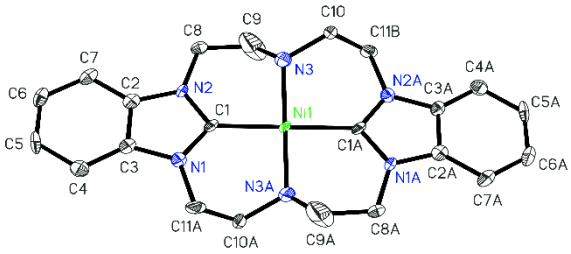

11a

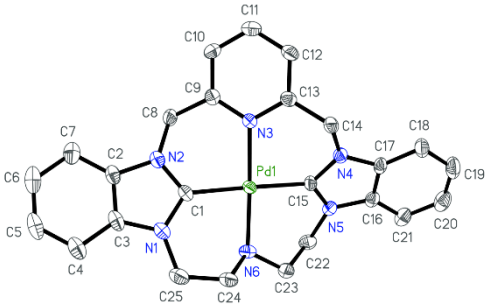

9

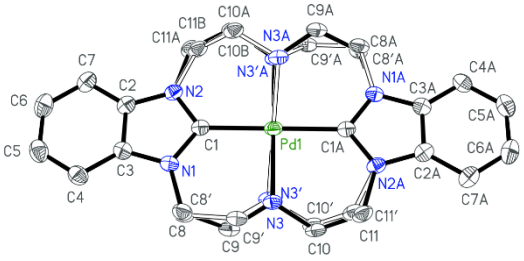

12a

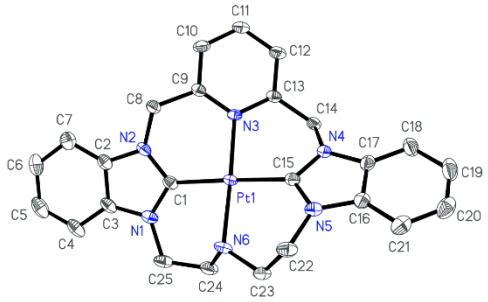

10

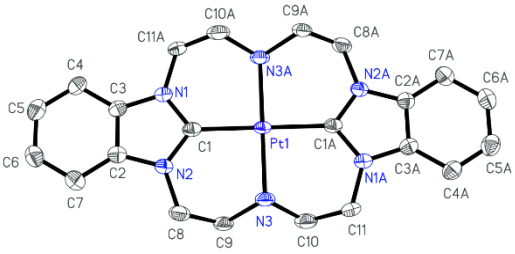

13a

Figure 4.3 Crystal structure of **8-13**, hydrogen atoms are omitted for clarity.

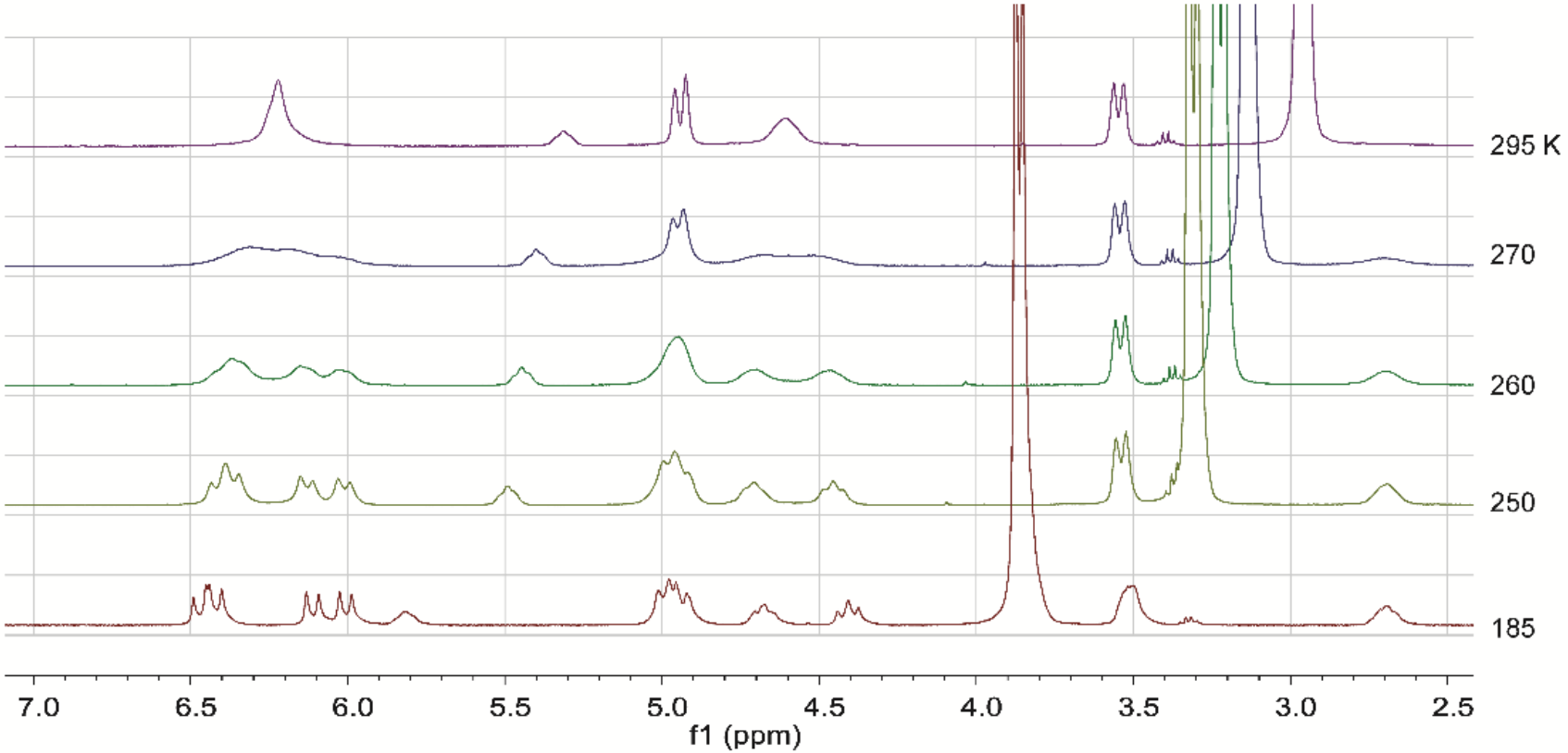

Figure 4.4 VT ^{1}H NMR spectra of **8** in acetone-d_6 (400 MHz).

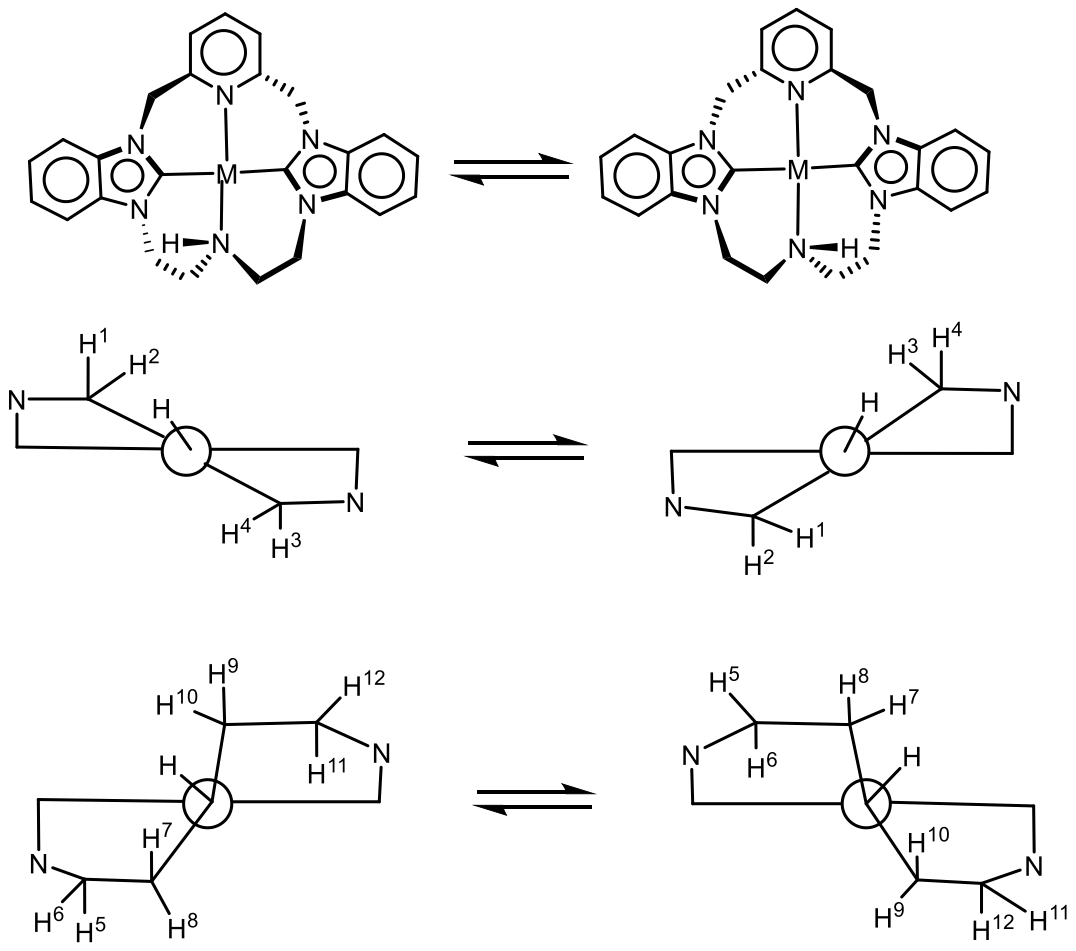

Figure 4.5 Ring twisting process of **8**-**10**. The Newman projects are viewed along the secondary amine-metal bond.

at 295 K. This peak also reaches its decoalescence at 270 K and yields a $\Delta G^{\ddagger}$ = 12.9 kcal mol^{-1}, which suggests peaks at 4.62 and 6.23 ppm are originated from the same dynamic process. It is noticed that two sets of singles are observed for the ethylene linker due to the effect of the secondary amine proton. Protons 5-12, 6-11, 7-10, 8-9 on the ethylene linker form four mutual exchange pairs when the molecule undergoes ring twisting process. The exchange of each pair yields one average signal at high temperature and two separated peaks at low temperature. Similar dynamics behavior is also observed in **9** and **10** (**Figures 4.6, 4.7**). The ring twisting process in **9** and **10** are much faster than that of in **8**. The averaged peak of **10** reaches its decoalescence at 190 K while the peak splitting of **9** is not complete even at 185 K.

Two sets of signals were observed at ^{1}H NMR spectra of the ethylene linkers in **11**–**13**, implying there are two conformers for each compound in solution. As proposed in **Figure 4.8**, depending on the different orientations of the secondary amine-hydrogen bond relative to the ring plane, the chemical environment of the ethylene linker could be different. However, the VT ^{1}H NMR spectra show no temperature-dependent peaks at 185–295 K, which suggests that the exchange between conformers **11a**-**13a** and **11b**-**13b** in these conditions are slower than the NMR timescale. VT ^{1}H NMR spectra of **11** in deuterated DMSO are collected at 293–403 K. These high temperature spectra did not show exchange either, which implies that the exchange of two conformers are still slower than the NMR timescale even under 403 K. Single-crystal XRD shows only conformers **11a**-**13b** exist in solid state. ^{1}H NMR spectra of a series of fresh prepared solution of **11**-**13** were collected after different periods of waiting time. It has been observed that conformers **11a**-**13a** slowly convert to **11b**-**13b** in solution at room temperature and reach

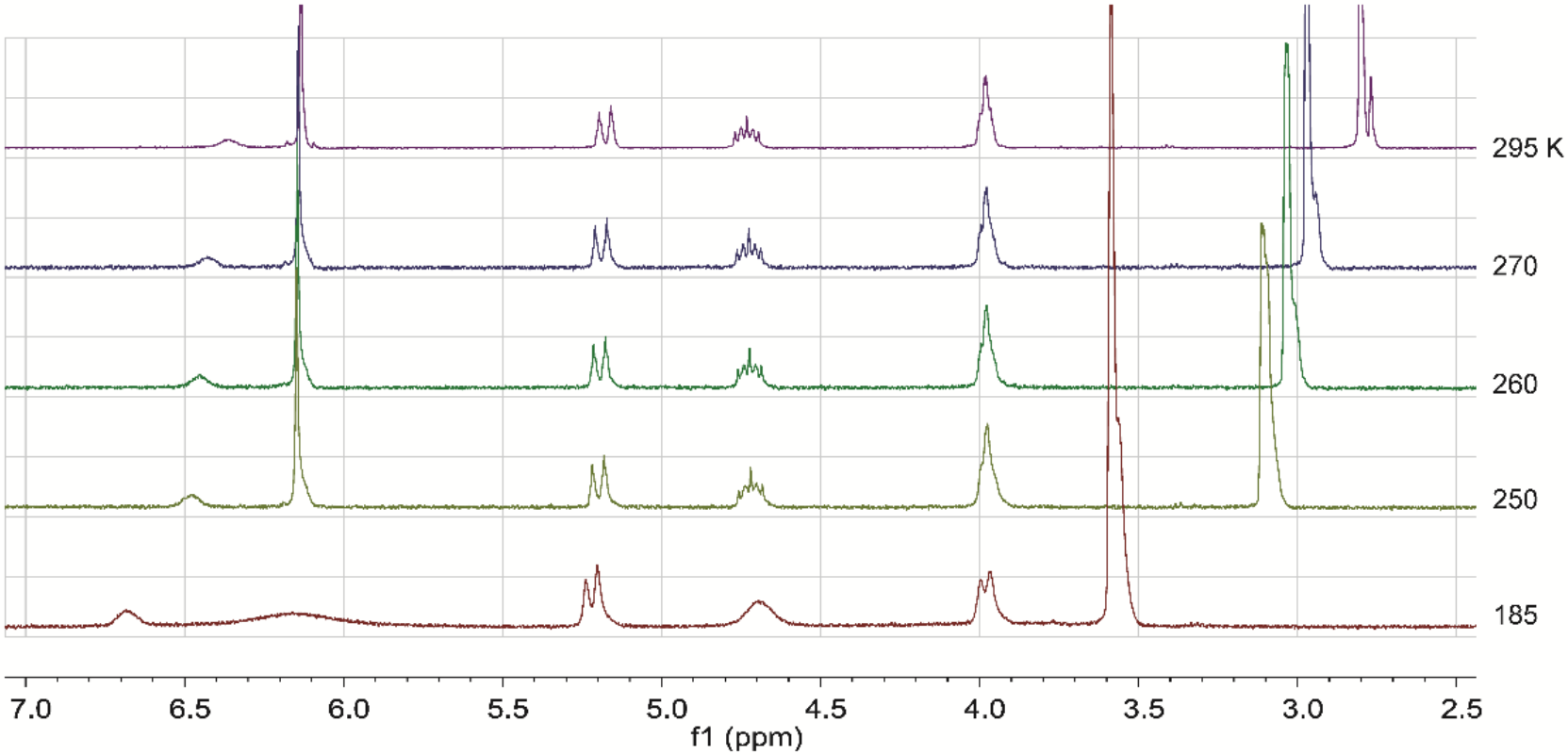

Figure 4.6 VT ^{1}H NMR spectra of **9** in acetone-d_6 (400 MHz).

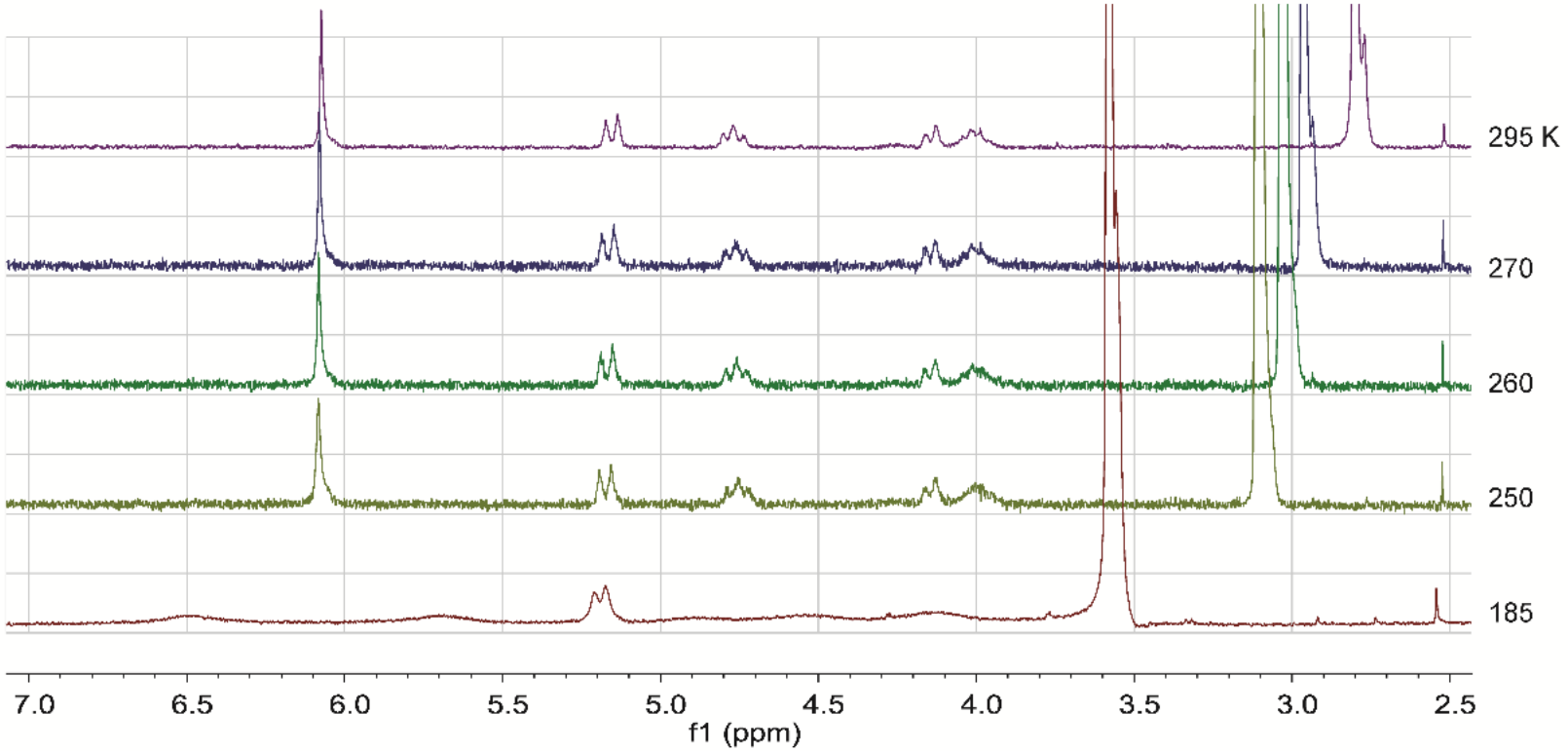

Figure 4.7 VT ^{1}H NMR spectra of **10** in acetone-d_6 (400 MHz).

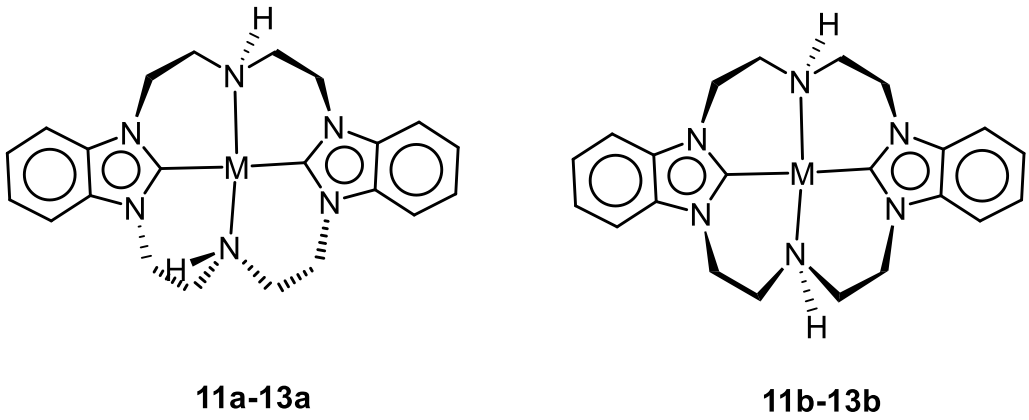

11a-13a **11b-13b**

Figure 4.8 Proposed two conformers of **11**-**13**.

equilibria in a couple of hours (**Figures 4.9**, **4.10**, and **4.11**).

Compound **14** is proofed to have static structure in solution by VT ^{1}H NMR.

4.4 Conclusion

In summary, seven macrocyclic amine-NHC metal complexes were extensively studied by different NMR spectroscopy techniques. The variable temperature ^{1}H NMR spectra have revealed an interconverting process between two atropisomers in **8**-**10** via ring twisting mechanism. This dynamic process happens within the timescale of NMR at 185-295 K. An interconverting between two achiral conformers in **11**-**13** was proposed for the mechanism of N-H bond orientation. This exchange could not be observed on variable temperature ^{1}H NMR spectra even at 403 K, indicating that this process is out of the range of the NMR timescale. The location of the ethylene linkers and a more planer structure of the macrocyclic ring might be the reason behind the slower dynamics of **11**-**13** compared to **8**-**10**.

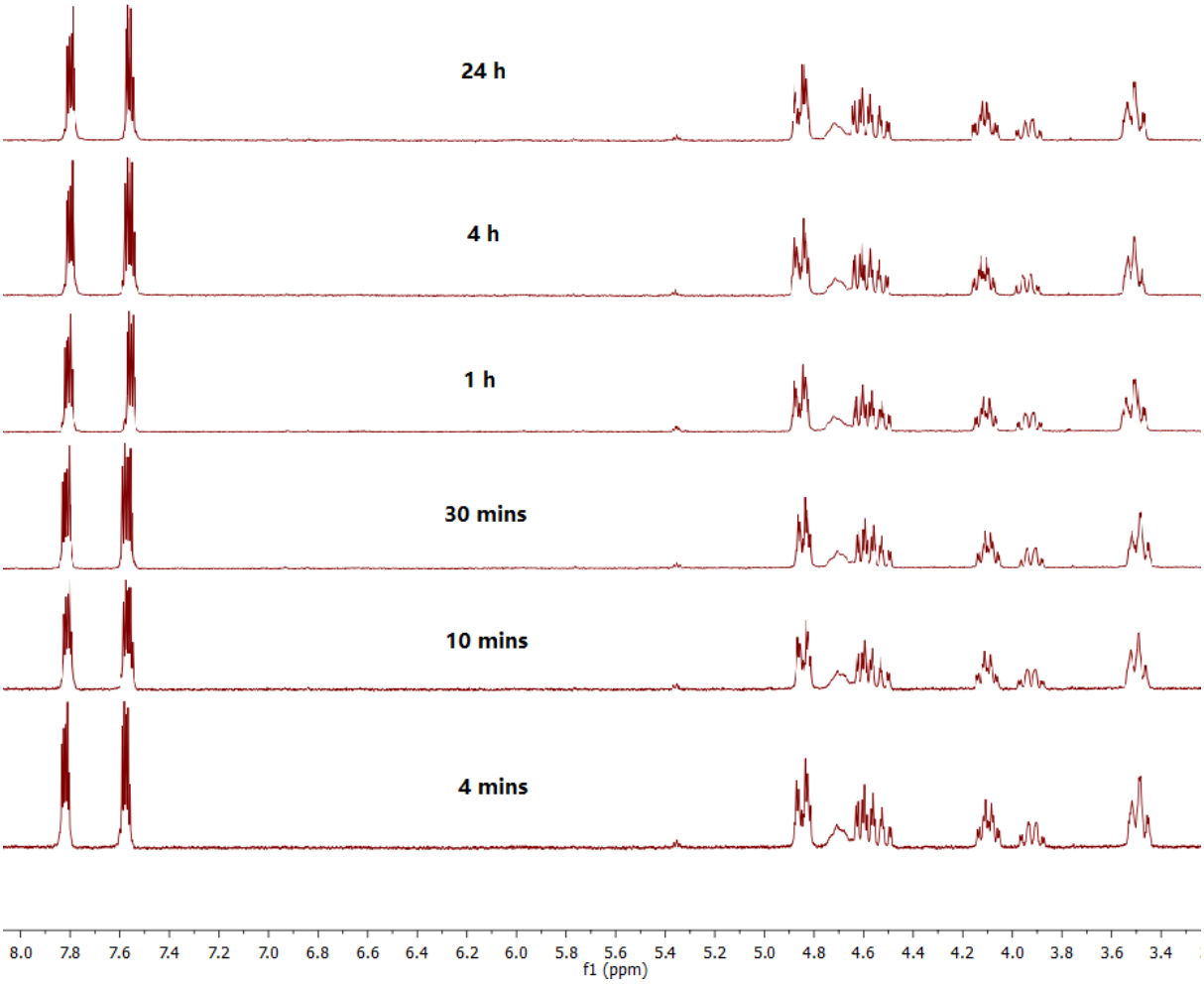

Figure 4.9 Time dependent ^{1}H NMR spectra of **11** (acetone-d_6, 400 MHz, 298 K).

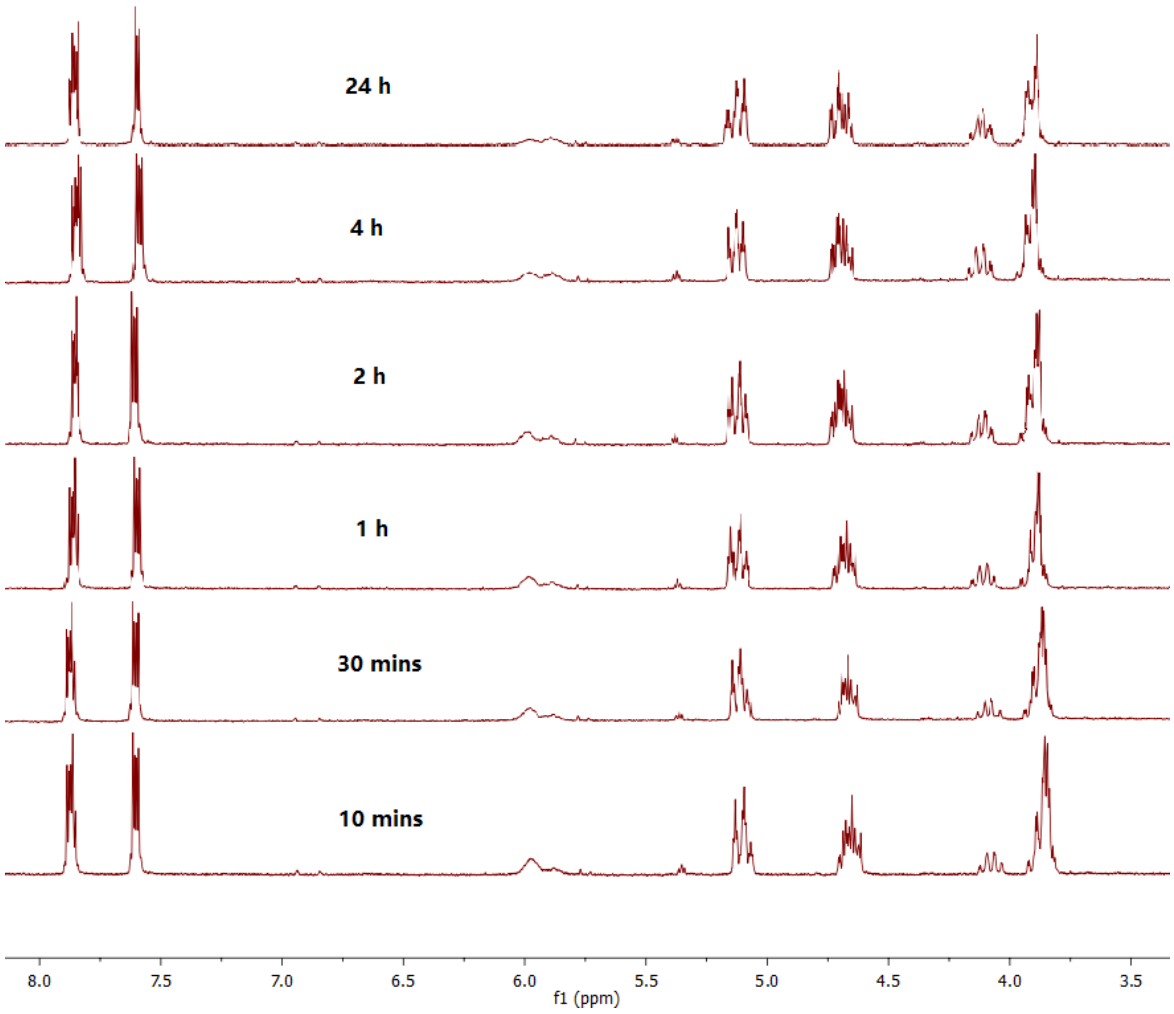

Figure 4.10 Time dependent ^{1}H NMR spectra of **12** (acetone-d_6, 400 MHz, 298 K).

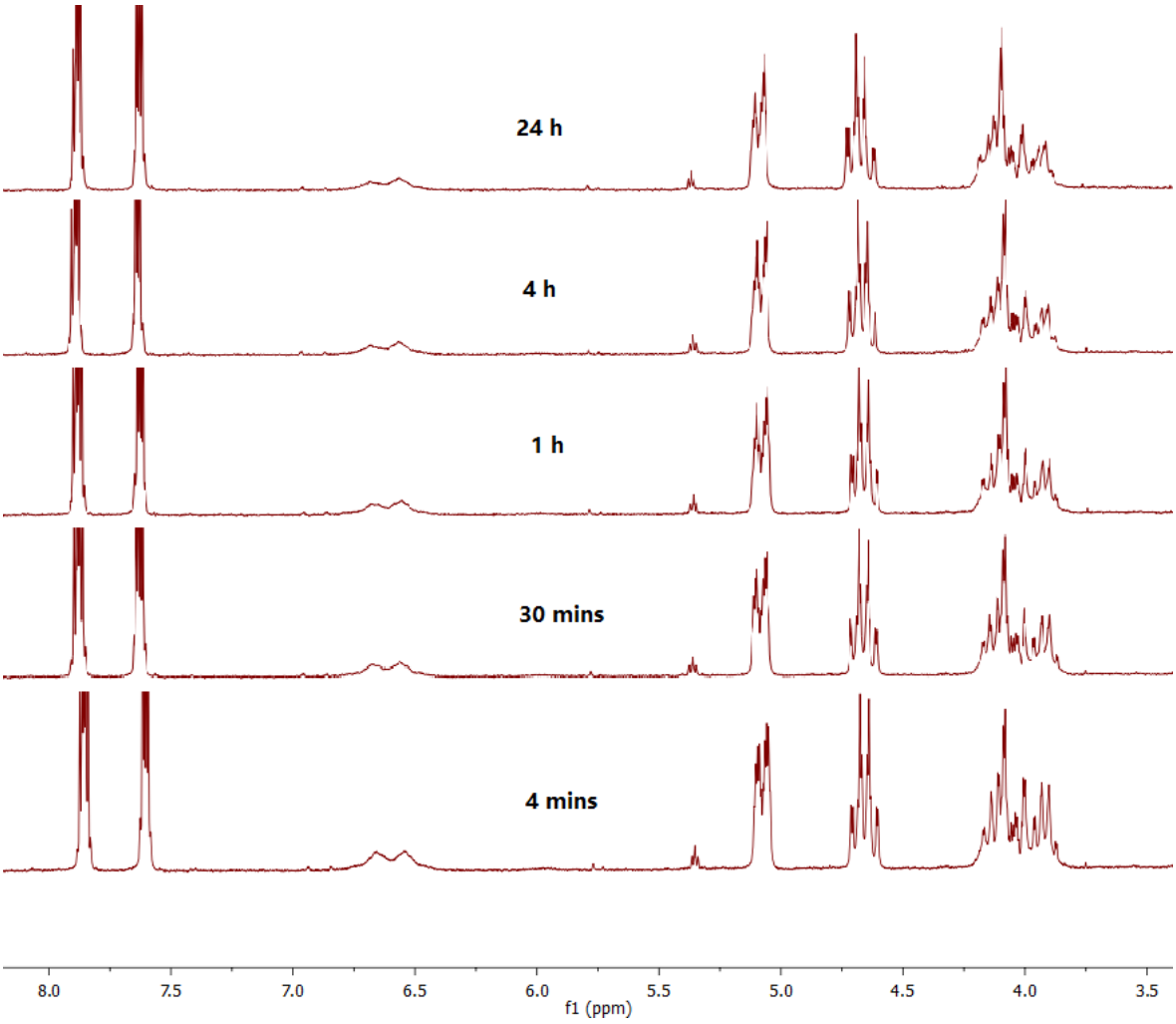

Figure 4.11 Time dependent ^{1}H NMR spectra of **13** (acetone-d_6, 400 MHz, 298 K).

References

1. Miller, J. S., Organic- and Molecule-Based Magnets. *Mater. Today* **2014,** *17*, 224.
2. Lucas, J.; Lucas, P.; Mercier, T. L.; Rollat, A.; Davenport, W. G., *Rare Earths: Science, Technology, Production and Use*. 2014.
3. Ritter, S. K., Single-Molecule Magnets Evolve. *Chem. Eng. News* **2004,** *82*, 29.
4. Sessoli, R.; Gatteschi, D.; Caneschi, A.; Novak, M. A., Magnetic Bistability in a Metal-Ion Cluster. *Nature* **1993,** *365*, 141.
5. Sessoli, R.; Tsai, H. L.; Schake, A. R.; Wang, S.; Vincent, J. B.; Folting, K.; Gatteschi, D.; Christou, G.; Hendrickson, D. N., High-Spin Molecules: $[Mn_{12}O_{12}(O_2CR)_{16}(H_2O)_4]$. *J. Am. Chem. Soc.* **1993,** *115*, 1804.
6. Guo, F.-S.; Day, B. M.; Chen, Y.-C.; Tong, M.-L.; Mansikkamäki, A.; Layfield, R. A., Magnetic Hysteresis Up to 80 Kelvin in a Dysprosium Metallocene Single-Molecule Magnet. *Science* **2018,** *362*, 1400.
7. Bunting, P. C.; Atanasov, M.; Damgaard-Møller, E.; Perfetti, M.; Crassee, I.; Orlita, M.; Overgaard, J.; van Slageren, J.; Neese, F.; Long, J. R., A Linear Cobalt(II) Complex with Maximal Orbital Angular Momentum from a Non-Aufbau Ground State. *Science* **2018,** *362*, 7319.
8. Rinehart, J. D.; Long, J. R., Exploiting Single-Ion Anisotropy in the Design of f-Element Single-Molecule Magnets. *Chem. Sci.* **2011,** *2*, 2078.
9. ETH-zurich Crystal-Field Splitting and Spin-Orbit Coupling. http://www.epr.ethz.ch/education/basic-concepts-of-epr/one-elect--in-the-magn--field/cf-split--so-coupl-.html.
10. Meng, Y.-S.; Jiang, S.-D.; Wang, B.-W.; Gao, S., Understanding the Magnetic Anisotropy toward Single-Ion Magnets. *Acc. Chem. Res.* **2016,** *49*, 2381.

11. Feng, M.; Tong, M.-L., Single Ion Magnets from 3d to 5f: Developments and Strategies. *Chem. Eur. J.* **2018,** *24*, 7574.
12. Frost, J. M.; Harriman, K. L. M.; Murugesu, M., The Rise of 3-d Single-Ion Magnets in Molecular Magnetism: Towards Materials from Molecules? *Chem. Sci.* **2016,** *7*, 2470.
13. Chen, Y.-C.; Liu, J.-L.; Wernsdorfer, W.; Liu, D.; Chibotaru, L. F.; Chen, X.-M.; Tong, M.-L., Hyperfine-Interaction-Driven Suppression of Quantum Tunneling at Zero Field in a Holmium(III) Single-Ion Magnet. *Angew. Chem. Int. Ed.* **2017,** *56*, 4996.
14. McAdams, S. G.; Ariciu, A.-M.; Kostopoulos, A. K.; Walsh, J. P. S.; Tuna, F., Molecular Single-Ion Magnets Based on Lanthanides and Actinides: Design Considerations and New Advances in the Context of Quantum Technologies. *Coord. Chem. Rev.* **2017,** *346*, 216.
15. Sivia, D. S., *Elementary scattering theory : for X-ray and neutron users*. 2011.
16. Carron, N. J., *An Introduction to the Passage of Energetic Particles through Matter*. 2007; p 308.
17. Hunter, S. C.; Podlesnyak, A. A.; Xue, Z.-L., Magnetic Excitations in Metalloporphyrins by Inelastic Neutron Scattering: Determination of Zero-Field Splittings in Iron, Manganese, and Chromium Complexes. *Inorg. Chem.* **2014,** *53*, 1955.
18. Xue, Z.-L.; Ramirez-Cuesta, A. J.; Brown, C. M.; Calder, S.; Cao, H.; Chakoumakos, B. C.; Daemen, L. L.; Huq, A.; Kolesnikov, A. I.; Mamontov, E.;

Podlesnyak, A. A.; Wang, X., Neutron Instruments for Research in Coordination Chemistry. *Eur. J. Inorg. Chem.* **2019,** 1065.

19. Disk Chopper Spectrometer (DCS). *NIST Center for Neutron Research* **2017**. https://www.nist.gov/ncnr/dcs-disk-chopper-spectrometer
20. Copley, J. R. D., *The Disk Chopper Spectrometer at NIST: The Good, the Bad and the Ugly*. 2005. https://www.ncnr.nist.gov/instruments/dcs/dcs_pdf_files/Copley2005_2.pdf
21. Cold Neutron Chopper Spectrometer. *Oak Ridge National Laboratory* **2017**. https://neutrons.ornl.gov/cncs
22. Ehlers, G.; Podlesnyak, A. A.; Kolesnikov, A. I., The cold neutron chopper spectrometer at the Spallation Neutron Source—A review of the first 8 years of operation. *Rev. Sci. Instrum.* **2016,** *87*, 93902.
23. Vibrational Spectrometer. *Oak Ridge National Laboratory* **2017**. https://neutrons.ornl.gov/vision
24. Seeger, P. A.; Daemen, L. L.; Larese, J. Z., Resolution of VISION, a crystal-analyzer spectrometer. *Nucl. Instrum. Methods Phys. Res. A.* **2009,** *604*, 719.
25. Roberts, J. D., *Nuclear Magnetic Resonance: Applications to Organic Chemistry*. 1959.
26. Reusch, W., *Supplemental NMR Topics*. 2013.
27. Powers, T. M. The Evans Method. https://www.jove.com/science-education/10304/the-evans-method.
28. Ostfeld, D.; Cohen, I. A., A Cautionary Note on the Use of the Evans Method for Magnetic Moments. *J. Chem. Educ.* **1972,** *49*, 829.

29. Elster, A. D. *Questions and Answers in NMR*. http://mriquestions.com/index.html.
30. Harris, D. C. A. R. K.; Hodgkinson, P., *Solid-State NMR: Basic Principles and Practice*. 2014.
31. Bren, K. L.; Eisenberg, R.; Gray, H. B., Discovery of the Magnetic Behavior of Hemoglobin: A Beginning of Bioinorganic Chemistry. *Proc. Natl. Acad. Sci. USA* **2015,** *112*, 13123.
32. Pauling, L.; Coryell, C. D., The Magnetic Properties and Structure of the Hemochromogens and Related Substances. *Proc. Natl. Acad. Sci. USA* **1936,** *22*, 159.
33. Pauling, L.; Coryell, C. D., The Magnetic Properties and Structure of Hemoglobin, Oxyhemoglobin and Carbonmonoxyhemoglobin. *Proc. Natl. Acad. Sci. USA* **1936,** *22*, 210.
34. Bren, K. L.; Eisenberg, R.; Gray, H. B., Discovery of the magnetic behavior of hemoglobin: A beginning of bioinorganic chemistry. *Proc. Natl. Acad. Sci. USA* **2015,** *112*, 13123.
35. Gatteschi, D.; Sessoli, R., Quantum Tunneling of Magnetization and Related Phenomena in Molecular Materials. *Angew. Chem. Int. Ed.* **2003,** *42*, 268.
36. Behere, D. V.; Mitra, S., Magnetic Susceptibility Study and Ground-State Zero-Field Splitting in Manganese(III) Porphyrins. *Inorg. Chem.* **1980,** *19*, 992.
37. Kennedy, B. J.; Murray, K. S., Magnetic Properties and Zero-Field Splitting in High-Spin Manganese(III) Complexes. 2. Axially Ligated Manganese(III) Porphyrin Complexes. *Inorg. Chem.* **1985,** *24*, 1557.

38. Pascual‐Álvarez, A.; Vallejo, J.; Pardo, E.; Julve, M.; Lloret, F.; Krzystek, J.; Armentano, D.; Wernsdorfer, W.; Cano, J., Field‐Induced Slow Magnetic Relaxation in a Mononuclear Manganese(III)–Porphyrin Complex. *Chem. Eur. J.* **2015,** *21*, 17299.
39. Duboc, C.; Ganyushin, D.; Sivalingam, K.; Collomb, M.-N.; Neese, F., Systematic Theoretical Study of the Zero-Field Splitting in Coordination Complexes of Mn(III). Density Functional Theory versus Multireference Wave Function Approaches. *J. Phys. Chem. A* **2010,** *114*, 10750.
40. Powell, M. F.; Pai, E. F.; Bruice, T. C., Study of (Tetraphenylporphinato)manganese(III)-Catalyzed Epoxidation and Demethylation Using *p*-Cyano-N,N-Dimethylaniline N-Oxide as Oxygen Donor in a Homogeneous System. Kinetics, Radiochemical Ligation Studies, and Reaction Mechanism for a Model of Cytochrome P-450. *J. Am. Chem. Soc.* **1984,** *106*, 3277.
41. Turner, P.; Gunter, M. J.; Skelton, B. W.; White, A. H., Crystal Structures of the Pentacoordinate Bromo, Isocyanato, Iodo, Acetato and Isothiocyanato Complexes of the meso-Tetraphenylporphyrinatomanganese Cation. *Aust. J. Chem.* **1998,** *51*, 835.
42. Krzystek, J.; Zvyagin, S. A.; Ozarowski, A.; Trofimenko, S.; Telser, J., Tunable-Frequency High-Field Electron Paramagnetic Resonance. *J. Magn. Reson.* **2006,** *178*, 174.

43. Goldberg, D. P.; Telser, J.; Krzystek, J.; Montalban, A. G.; Brunel, L.-C.; Barrett, A. G. M.; Hoffman, B. M., EPR Spectra from “EPR-Silent” Species: High-Field EPR Spectroscopy of Manganese(III) Porphyrins. *J. Am. Chem. Soc.* **1997,** *119*, 8722.
44. Krzystek, J.; Telser, J.; Pardi, L. A.; Goldberg, D. P.; Hoffman, B. M.; Brunel, L.-C., High-Frequency and -Field Electron Paramagnetic Resonance of High-Spin Manganese(III) in Porphyrinic Complexes. *Inorg. Chem.* **1999,** *38*, 6121.
45. Krzystek, J.; Pardi, L. A.; Brunel, L.-C.; Goldberg, D. P.; Hoffman, B. M.; Licoccia, S.; Telser, J., High-Frequency and -Field Electron Paramagnetic Resonance of High-Spin Manganese(III) in Tetrapyrrole Complexes. *Spectrochim. Acta A* **2002,** *58*, 1113.
46. Mossin, S.; Weihe, H.; Barra, A.-L., Is the Axial Zero-Field Splitting Parameter of Tetragonally Elongated High-Spin Manganese(III) Complexes Always Negative? *J. Am. Chem. Soc.* **2002,** *124*, 8764.
47. Ikeda, O.; Kojima, T.; Tamura, H., Effect of Axial Ligands on the Catalytic Activity of Meso-Tetraphenylporphyrinatomanganese(III) Halides in the Cathodic Reduction of Oxygen. *J. Electroanal. Chem.* **1986,** *200*, 323.
48. Pascual-Álvarez, A.; Vallejo, J.; Pardo, E.; Julve, M.; Lloret, F.; Krzystek, J.; Armentano, D.; Wernsdorfer, W.; Cano, J., Field-Induced Slow Magnetic Relaxation in a Mononuclear Manganese(III)–Porphyrin Complex. *Chem. Eur. J.* **2015,** *21*, 17299.
49. Gary L. Miessler, P. J. F., Donald A. Tarr, *Inorganic Chemistry, 5th Edition*. 2014.

50. Turner, P.; Gunter, M. J., Carbon-13 NMR Spectroscopy, Electron Spin Distribution, and Valence State of Pentacoordinate Manganese Tetraphenylporphyrin Complexes. *Inorg. Chem.* **1994,** *33*, 1406.
51. Duer, M. J., *Solid-State NMR Spectroscopy: Principles and Applications*. 2002.
52. Wu, S. Introduction to Solid-state NMR. http://www.emory.edu/NMR/web_swu/SSNMR_redor/ssnmr_schurko.
53. Pedersen, K. S.; Sørensen, M. A.; Bendix, J., Fluoride-Coordination Chemistry in Molecular and Low-Dimensional Magnetism. *Coord. Chem. Rev.* **2015,** *299*, 1.
54. Birk, T.; Pedersen, K. S.; Piligkos, S.; Thuesen, C. A.; Weihe, H.; Bendix, J., Magnetic Properties of a Manganese(III) Chain with Monoatomic Bridges: catena-MnF(salen). *Inorg. Chem.* **2011,** *50*, 5312.
55. Čižmár, E.; Risset, O. N.; Wang, T.; Botko, M.; Ahir, A. R.; Andrus, M. J.; Park, J.-H.; Abboud, K. A.; Talham, D. R.; Meisel, M. W.; Brown, S. E., Antiferromagnetic Ordering in MnF(salen). *J. Phys. Condens. Matter* **2016,** *28*, 236003.
56. Goodwin, C. A. P.; Ortu, F.; Reta, D.; Chilton, N. F.; Mills, D. P., Molecular Magnetic Hysteresis at 60 Kelvin in Dysprosocenium. *Nature* **2017,** *548*, 439.
57. Goodwin, C. A. P.; Reta, D.; Ortu, F.; Chilton, N. F.; Mills, D. P., Synthesis and Electronic Structures of Heavy Lanthanide Metallocenium Cations. *J. Am. Chem. Soc.* **2017,** *139*, 18714.
58. Guo, F.-S.; Day, B. M.; Chen, Y.-C.; Tong, M.-L.; Mansikkamäki, A.; Layfield, R. A., A Dysprosium Metallocene Single-Molecule Magnet Functioning at the Axial Limit. *Angew. Chem. Int. Ed.* **2017,** *56*, 11445.

59. Karunadasa, H. I.; Arquero, K. D.; Berben, L. A.; Long, J. R., Enhancing the Magnetic Anisotropy of Cyano-Ligated Chromium(II) and Chromium(III) Complexes via Heavy Halide Ligand Effects. *Inorg. Chem.* **2010,** *49*, 4738.
60. Goswami, T.; Misra, A., Ligand Effects toward the Modulation of Magnetic Anisotropy and Design of Magnetic Systems with Desired Anisotropy Characteristics. *J. Phys. Chem. A* **2012,** *116*, 5207.
61. Ye, S.; Neese, F., How Do Heavier Halide Ligands Affect the Signs and Magnitudes of the Zero-Field Splittings in Halogenonickel(II) Scorpionate Complexes? A Theoretical Investigation Coupled to Ligand-Field Analysis. *J. Chem. Theory Comput.* **2012,** *8*, 2344.
62. Zadrozny, J. M.; Telser, J.; Long, J. R., Slow Magnetic Relaxation in the Tetrahedral Cobalt(II) Complexes $[Co(EPh)_4]^{2-}$ (E = O, S, Se). *Polyhedron* **2013,** *64*, 209-217.
63. Saber, M. R.; Dunbar, K. R., Ligands effects on the magnetic anisotropy of tetrahedral cobalt complexes. *Chem. Commun.* **2014,** *50*, 12266.
64. Yang, F.; Zhou, Q.; Zhang, Y.-Q.; Zeng, G.; Li, G.; Shi, Z.; Wang, B.; Feng, S., Inspiration from Old Molecules: Field-Induced Slow Magnetic Relaxation in Three Air-Stable Tetrahedral Cobalt(II) Compounds. *Chem. Commun.* **2013,** *49*, 5289.
65. Boča, R.; Miklovič, J.; Titiš, J., Simple Mononuclear Cobalt(II) Complex: A Single-Molecule Magnet Showing Two Slow Relaxation Processes. *Inorg. Chem.* **2014,** *53*, 2367.

66. Krzystek, J.; Zvyagin, S. A.; Ozarowski, A.; Fiedler, A. T.; Brunold, T. C.; Telser, J., Definitive Spectroscopic Determination of Zero-Field Splitting in High-Spin Cobalt(II). *J. Am. Chem. Soc.* **2004,** *126*, 2148.
67. Azuah, R. T.; Kneller, L. R.; Qiu, Y.; Tregenna-Piggott, P. L. W.; Brown, C. M.; Copley, J. R. D.; Dimeo, R. M., DAVE: A Comprehensive Software Suite for the Reduction, Visualization, and Analysis of Low Energy Neutron Spectroscopic Data. *J. Res. Natl. Inst. Stand. Technol.* **2009,** *114*, 341.
68. Giansiracusa, M. J.; Vonci, M.; Van den Heuvel, W.; Gable, R. W.; Moubaraki, B.; Murray, K. S.; Yu, D.; Mole, R. A.; Soncini, A.; Boskovic, C., Carbonate-Bridged Lanthanoid Triangles: Single-Molecule Magnet Behavior, Inelastic Neutron Scattering, and Ab Initio Studies. *Inorg. Chem.* **2016,** *55*, 5201.
69. Colacio, E.; Ruiz, J.; Ruiz, E.; Cremades, E.; Krzystek, J.; Carretta, S.; Cano, J.; Guidi, T.; Wernsdorfer, W.; Brechin, E. K., Slow Magnetic Relaxation in a Co^{II}–Y^{III} Single-Ion Magnet with Positive Axial Zero-Field Splitting. *Angew. Chem. Int. Ed.* **2013,** *52*, 9130.
70. Eastman, K. J., N-Heterocyclic Carbenes (NHCs). *Scripps Research*.
71. Arduengo, A. J.; Harlow, R. L.; Kline, M., A Stable Crystalline Carbene. *J. Am. Chem. Soc.* **1991,** *113*, 361.
72. Poyatos, M.; Mata, J. A.; Peris, E., Complexes with Poly(N-heterocyclic carbene) Ligands: Structural Features and Catalytic Applications. *Chem. Rev.* **2009,** *109*, 3677.
73. Díez-González, S.; Marion, N.; Nolan, S. P., N-Heterocyclic Carbenes in Late Transition Metal Catalysis. *Chem. Rev.* **2009,** *109*, 3612.

74. Sinha, N.; Hahn, F. E., Metallosupramolecular Architectures Obtained from Poly-N-heterocyclic Carbene Ligands. *Acc. Chem. Res.* **2017,** *50*, 2167.
75. Mercs, L.; Albrecht, M., Beyond Catalysis: N-Heterocyclic Carbene Complexes as Components for Medicinal, Luminescent, and Functional Materials Applications. *Chem. Soc. Rev.* **2010,** *39*, 1903.
76. Bertrand, B.; Citta, A.; Franken, I.; Picquet, M.; Folda, A.; Scalcon, V.; Rigobello, M.; Gendre, P.; Casini, A.; Bodio, E., Gold(I) NHC-Based Homo- and Heterobimetallic Complexes: Synthesis, Characterization and Evaluation as Potential Anticancer Agents. *J. Biol. Inorg. Chem.* **2015,** *20*, 1005.
77. Hindi, K. M.; Panzner, M. J.; Tessier, C. A.; Cannon, C. L.; Youngs, W. J., The Medicinal Applications of Imidazolium Carbene−Metal Complexes. *Chem. Rev.* **2009,** *109*, 3859.
78. Cabbiness, D. K.; Margerum, D. W., Macrocyclic Effect on the Stability of Copper(II) Tetramine Complexes. *J. Am. Chem. Soc.* **1969,** *91*, 6540.
79. Garrison, J. C.; Simons, R. S.; Talley, J. M.; Wesdemiotis, C.; Tessier, C. A.; Youngs, W. J., Synthesis and Structural Characterization of an Imidazolium-Linked Cyclophane and the Silver Complex of an N-Heterocyclic Carbene-Linked Cyclophane. *Organometallics* **2001,** *20*, 1276.
80. Baker, M. V.; Skelton, B. W.; White, A. H.; Williams, C. C., Synthesis and Characterization of a Saddle-Shaped Nickel−Carbene Complex Derived from an Imidazolium-Linked meta-Cyclophane. *Organometallics* **2002,** *21*, 2674.

81. Klawitter, I.; Anneser, M. R.; Dechert, S.; Meyer, S.; Demeshko, S.; Haslinger, S.; Pöthig, A.; Kühn, F. E.; Meyer, F., Iron Complexes of a Macrocyclic N-Heterocyclic Carbene/Pyridine Hybrid Ligand. *Organometallics* **2015,** *34*, 2819.
82. Flores-Figueroa, A.; Pape, T.; Feldmann, K.-O.; Hahn, F. E., Template-Controlled Synthesis of a Planar [16]ane-$P_2C^{NHC}_2$ Macrocycle. *Chem. Commun.* **2010,** *46*, 324.
83. Anneser, M. R.; Haslinger, S.; Pöthig, A.; Cokoja, M.; D'Elia, V.; Högerl, M. P.; Basset, J.-M.; Kühn, F. E., Binding of Molecular Oxygen by an Artificial Heme Analogue: Investigation on the Formation of an Fe–Tetracarbene Superoxo Complex. *Dalton Trans.* **2016,** *45*, 6449.
84. Beattie, J. K., Conformational Analysis of Tris(ethylenediamine) Complexes. *Acc. Chem. Res.* **1971,** *4*, 253.
85. Altmann, P. J.; Weiss, D. T.; Jandl, C.; Kühn, F. E., Exploring Coordination Modes: Late Transition Metal Complexes with a Methylene-Bridged Macrocyclic Tetra-NHC Ligand. *Chem. Asian J.* **2016,** *11*, 1597.

Appendix

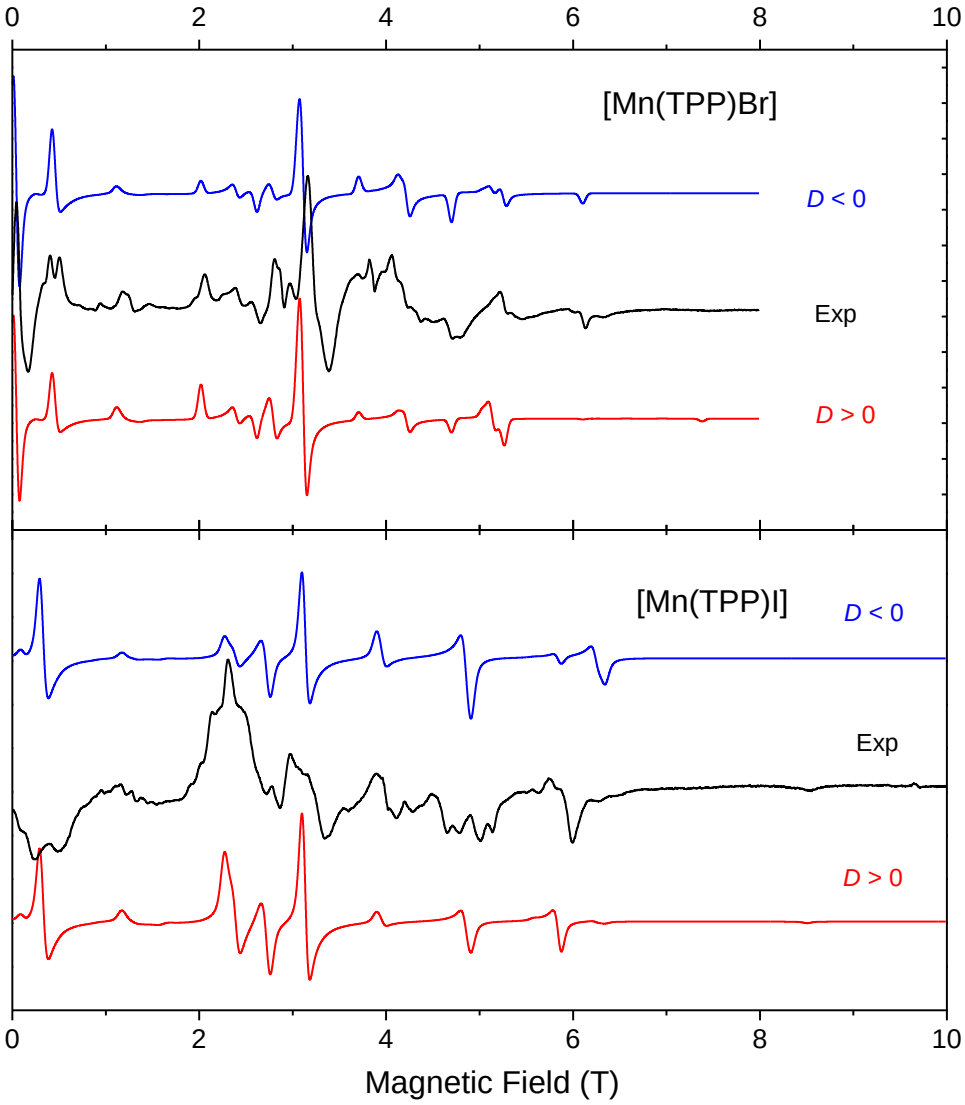

Figure S-1 HF-EPR spectra of **1** (Top) and **2** (Bottom) at 10 K and 108 and 112 GHz, respectively (black traces) and their powder-pattern simulations (colored traces). The spin Hamiltonian parameters used in simulations were the same as in **Table 2.1**. Blue traces: $D < 0$; red traces: $D > 0$.

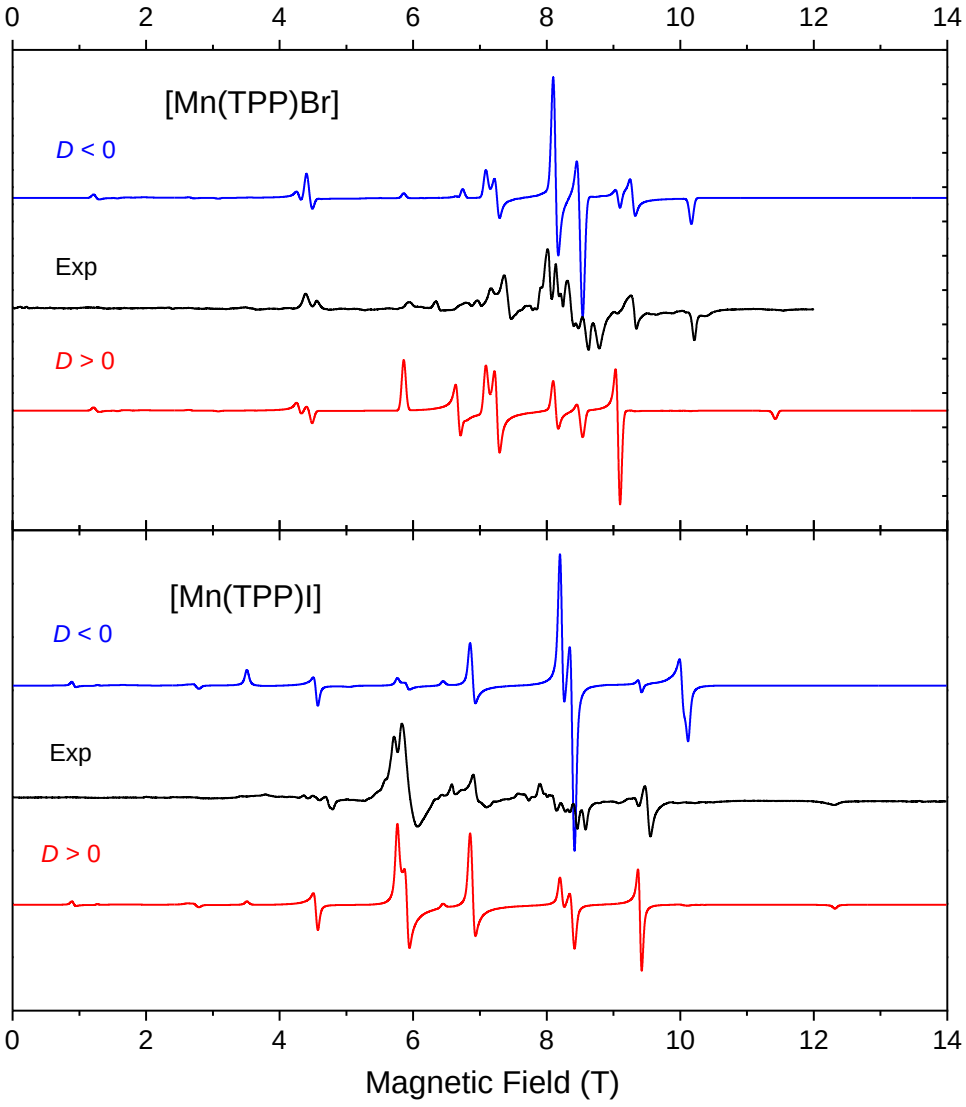

Figure S-2 HF-EPR spectra of **1** (Top) and **2** (Bottom) at 10 K and 216 and 220.8 GHz, respectively (black traces) and their powder-pattern simulations (colored traces). The spin Hamiltonian parameters used in simulations were the same as in **Table 2.1**. Blue traces: $D < 0$; red traces: $D > 0$.

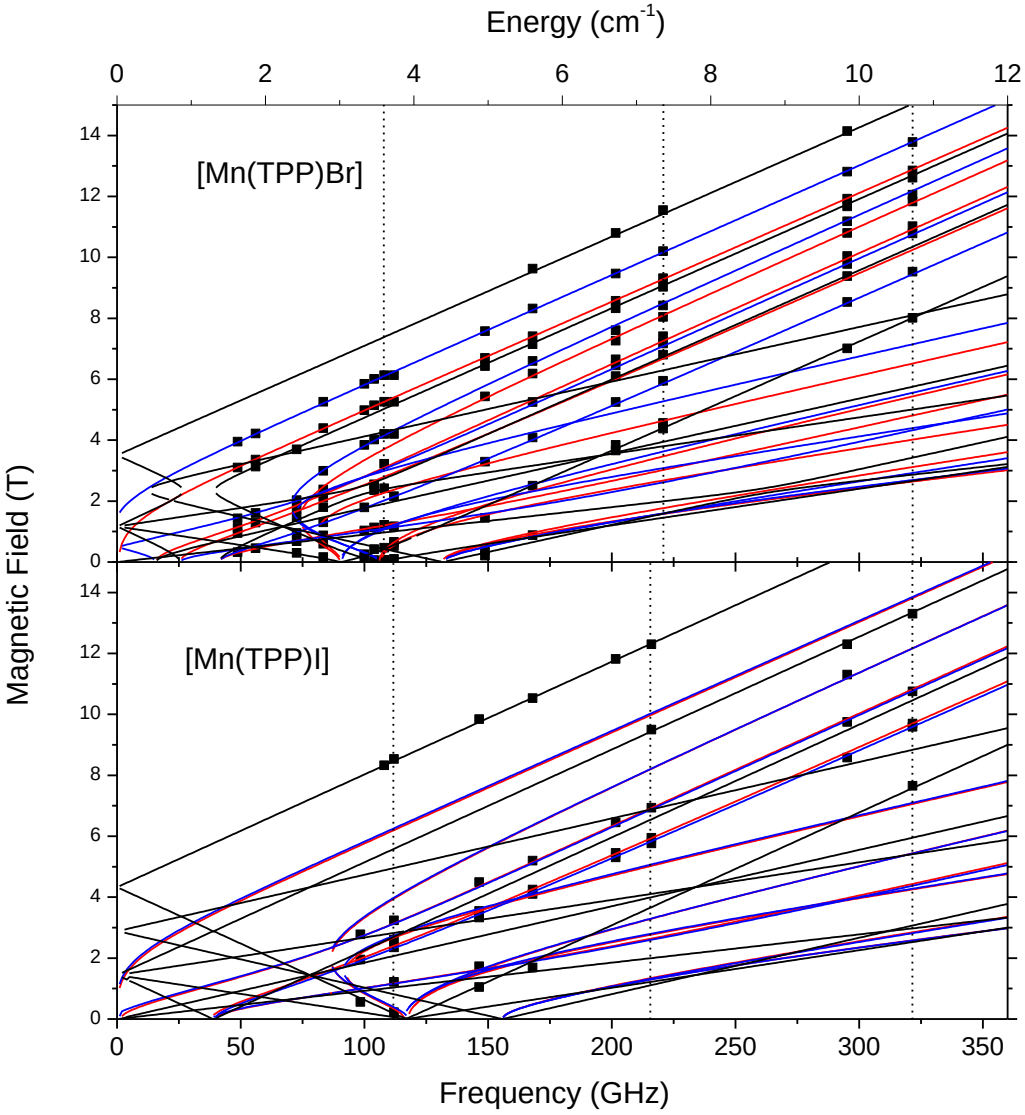

Figure S-3 2-D field/frequency (energy) maps of turning points in HF-EPR spectra of **1** (Top) and **2** (Bottom, black squares in each case). The curves are simulations using spin Hamiltonian parameters as in **Table 2.1**. Red curves: turning points with magnetic field parallel to the *x* axis of the ZFS tensor, blue: B_0 || *y*; black: B_0 || *z*. Off-axis turning points, of which there are several depending on frequency, are not plotted as they were not used in the fits. The vertical dashed lines represent frequencies.

Vita

Zhiming Liu was born in Weihai, Shandong, China. He enrolled in Jiangnan University in 2012 and graduated with B.S. (Honors) degree in Applied Chemistry in 2016. He was an exchange student in the Department of Chemistry, University of Tennessee-Knoxville (UTK), in 2014-2015 semester. Liu conducted undergraduate research with Dr. Zhiguo Gu (Jiangnan University) on synthesis and characterization of spin-crossover complexes and Dr. Sheng Dai (UTK) on surface modification of mesoporous carbon for CO_2 caption. He began his graduate studies in inorganic chemistry at UTK in August 2016.